Atmos. Chem. Phys. Discuss., doi:10.5194/acp-2015-924, 2016
Manuscript under review for journal Atmos. Chem. Phys.
Published: 1 February 2016

Atmospheric Chemistry and Physics Discussions

Impact of Spaceborne Carbon Monoxide Observations from the S-5P platform on Tropospheric Composition Analyses and Forecasts

R. Abida[1], J.-L. Attié[1,2], L. El Amraoui[1], P. Ricaud[1], W. Lahoz[3], H. Eskes[4], A. Segers[5], L. Curier[5], J. de Haan[4], J. Kujanpää[6], A. O. Nijhuis[4], D. Schuettemeyer[7], J. Tamminen[6], R. Timmermans[5], P. Veefkind[4], and B. Veihelmann[7]

[1] CNRM-GAME, Météo-France/CNRS UMR 3589, Toulouse, France
[2] Université de Toulouse, Laboratoire d'Aérologie, CNRS UMR 5560, Toulouse, France
[3] NILU – Norwegian Institute for Air Research, P.O. Box 100, 2027 Kjeller, Norway
[4] Royal Netherlands Meteorological Institute (KNMI), P.O. Box 201, 3730 AE De Bilt, The Netherlands
[5] TNO, Business unit Environment, Health and Safety, P.O. Box 80015, 3508 TA Utrecht, The Netherlands
[6] Finnish Meteorological Institute, Earth Observation Unit, P.O. Box 503, 00101 Helsinki, Finland
[7] ESA/ESTEC, Earth Observation Programmes, Noordwijk, The Netherlands

Submitted to Atmospheric Chemistry and Physics Discussions, 13 November 2015

Atmos. Chem. Phys. Discuss., doi:10.5194/acp-2015-924, 2016
Manuscript under review for journal Atmos. Chem. Phys.
Published: 1 February 2016

Atmospheric Chemistry and Physics Discussions

Abstract

We use the technique of Observing System Simulation Experiments (OSSEs) to quantify the impact of spaceborne carbon monoxide (CO) total column observations from the Sentinel-5 Precursor (S-5P) platform on tropospheric analyses and forecasts. We focus on Europe for the period of northern summer 2003, when there was a severe heat wave episode associated with extremely hot and dry weather conditions. We describe different elements of the OSSE: (i) the Nature Run (NR), i.e., the "Truth"; ii) the CO synthetic observations; (iii) the assimilation run (AR), where we assimilate the observations of interest; (iv) the control run (CR), in this study a free model run without assimilation; and (v) efforts to establish the fidelity of the OSSE results. Comparison of the results from AR and the CR, against the NR, shows that CO total column observations from S-5P provide a significant benefit (at the 99% confidence level) at the surface, with the largest benefit occurring over land in remote regions. Furthermore, the S-5P CO total column observations are able to capture phenomena such as the forest fires that occurred in Portugal during summer 2003. These results provide evidence of the benefit of S-5P observations for monitoring processes contributing to atmospheric pollution.

Atmos. Chem. Phys. Discuss., doi:10.5194/acp-2015-924, 2016
Manuscript under review for journal Atmos. Chem. Phys.
Published: 1 February 2016

Atmospheric Chemistry and Physics Discussions

1. Introduction

Over the last decade, the capabilities of satellite instruments for sensing the lower troposphere have improved, and opened the way for monitoring and better understanding of atmospheric pollution processes, e.g., tropospheric chemistry (Jacob, 2000), long-range transport (HTAP, 2007), and emissions (e.g. Streets D., 2013 and references therein). Satellite instruments provide global measurements of many pollutants (e.g., ozone; carbon monoxide, CO; nitrogen dioxide, NO_2; and aerosols), including information on their trans-boundary transport, and complement in situ measurements from ground-based stations (e.g., the EMEP, http://www.nilu.no/projects/ccc/emepdata.html, and Airbase, http://acm.eionet.europa.eu/databases/airbase/, networks). Low Earth Orbit (LEO) satellite platforms have the advantage of providing observations with global coverage, but at a relatively low temporal resolution. Geostationary Earth Orbit (GEO) satellite platforms provide observations at a continental scale, i.e., not global, but at a much higher temporal resolution.

Satellite data, either in synergy with ground-based and airborne measurements and/or assimilated into models such as chemistry transport models (CTMs), contribute to an improved understanding of tropospheric chemistry and dynamics and improved forecasts of atmospheric pollutant fields (see, e.g., Elbern et al., 2010). As part of an integrated observing strategy, satellite measurements provide a global view on air quality (AQ). The challenge for future space-borne missions will be to assess directly the local scales of transport and/or chemistry for tropospheric pollutants (1 hour or less, 10 km or less) and to facilitate the use of remote sensing information for improving local- and regional-scale (from country-wide to continental scales) AQ analyses and forecasts. Building on this effort, various LEO satellite platforms and/or constellations of GEO satellite platforms will help extend AQ information from continental scales to global scales (e.g., Lahoz et al., 2012, and references therein for LEO/GEO platforms; Barré et al., 2015, for GEO platforms).

An atmospheric species of interest for monitoring AQ is CO, owing to its relatively long time-scale in the troposphere; its distribution provides information on the transport pathways of atmospheric pollutants. Spaceborne instruments on LEO satellite platforms demonstrate the potential of remote sensing from space

Atmos. Chem. Phys. Discuss., doi:10.5194/acp-2015-924, 2016
Manuscript under review for journal Atmos. Chem. Phys.
Published: 1 February 2016

Atmospheric Chemistry and Physics Discussions

to determine the CO distribution and its main emission sources at the global scale (Edwards et al., 2004, 2006; Buchwitz et al., 2006; Worden et al., 2013 and references therein). These LEO satellite platforms include MOPITT (Measurements Of Pollution In The Troposphere), IASI (Infrared Atmospheric Sounding Interferometer), AIRS (Atmospheric InfraRed Sounder) and TES (Tropospheric Emission Spectrometer) operating in the thermal infrared (TIR) and SCIAMACHY (SCanning Imaging Absorption spectroMeter for Atmospheric ChartographY) operating in the short-wave infrared (SWIR), respectively. By contrast, to our knowledge, there are no GEO satellite platforms measuring the CO distribution. However, despite their potential, owing to limited revisit time, and relatively coarse spatial resolution, LEO instruments are not optimal for monitoring regional and local aspects of air quality.

Copernicus is the current European Programme for the establishment of a European capability for Earth Observation (http://www.copernicus.eu/pages-principales/services/atmosphere-monitoring). The main objective of the Copernicus Atmospheric Services is to provide information on atmospheric variables (e.g., the essential climate variables, ECVs; https://www.wmo.int/pages/prog/gcos/index.php?name=EssentialClimateVariables) in support of European policies regarding sustainable development and global governance of the environment. The Copernicus Atmospheric Services cover: AQ, climate change/forcing, stratospheric ozone and solar radiation. The services rely mainly on data from Earth Observation satellites.

To ensure operational provision of Earth Observation data, the space component of the Copernicus programme includes a series of spaceborne missions developed and managed by the European Space Agency (ESA) and EUMETSAT. Among them, three missions address atmospheric composition. These are the Sentinel-5 (S-5) and Sentinel-5 Precursor (S-5P) from a LEO satellite platform, and the Sentinel-4 (S-4) from a GEO satellite platform. The goal of the S-4 is to monitor key atmospheric pollutants (e.g., ozone; NO_2; sulphur dioxide, SO_2; bromine monoxide, BrO; and formaldehyde) and aerosols at relatively high spatio-temporal resolution over Europe and North Africa (8 km; 1 hour). The goal of the S-5 and S-5P platforms is to provide global daily measurements of atmospheric pollutants (e.g., CO, ozone, NO_2, SO_2, BrO, and formaldehyde), climate related trace gases (e.g., methane, CH_4) and aerosols, at relatively high spatial resolution (from below 8 km to below 50 km, depending on wavelength).

Atmos. Chem. Phys. Discuss., doi:10.5194/acp-2015-924, 2016
Manuscript under review for journal Atmos. Chem. Phys.
Published: 1 February 2016

The S-5P is the ESA pre-operational mission required to bridge the gap between the end of the OMI (Ozone Monitoring Instrument) and the SCIAMACHY missions and the start of the S-5 mission planned for 2020 onwards. The S-5P scheduled launch is in 2016 with a 7 years design lifetime. The S-5P will fly in an early afternoon sun-synchronous LEO geometry with an Equator crossing mean local solar time of 13:30, chosen to allow the instrument to measure the strong pollution signal present in the afternoon. In contrast, the GOME-2 (Global Ozone Monitoring Experiment - 2) platform collects data at a local solar time of 09:30 (when the pollution signal is relatively weak) and thus has a lower predictive value (Veefkind et al., 2012, and references therein). The S-5P LEO platform will address the challenge of limited revisit time from LEOs by providing unprecedented high spatial resolution of 7x7 km, and improved sensitivity in the Planetary Boundary Layer (PBL), allowing resolution of, e.g., derived CO emission sources at finer scales than hitherto. The PBL varies in depth throughout the year, but is contained within the lowermost troposphere (heights 0-3 km), and typically spans the heights 0-1 km.

A method to objectively determine the added value of future satellite observations such as S-4, S-5 and S-5P, and to investigate the impact of different instrument designs, is that of Observing System Simulation Experiments (OSSEs) commonly based on data assimilation (e.g., Lahoz and Schneider, 2014). The OSSEs have been extensively used and shown to be useful in the meteorological community to test the impact of future meteorological observations on the quality of weather forecasts (Nitta, 1975; Atlas, 1997; Lord et al., 1997; Atlas et al., 2003). In a recent paper, Timmermans et al. (2015) review the application of OSSEs to assess future missions to monitor AQ. The OSSEs are increasingly being used by the space agencies to assess the added value of future instruments to be deployed as part of the Global Observing System (e.g., work on the ESA Earth Explorer ADM-Aeolus; Tan et al., 2007).

Although the usefulness of OSSEs is well established, they have limitations, discussed in Masutani et al. (2010a, b). A frequent criticism of OSSEs is that they are overoptimistic, largely owing to the difficulties of representing the real Earth System (e.g., the atmosphere), even with state-of-the-art numerical models. Nevertheless, even if overoptimistic, OSSEs provide bounds on the impact of new observing systems. For example, if additional instruments provide no significant impact within an OSSE, they are unlikely to do so in reality.

121

122 In this paper, we describe a regional-scale OSSE over Europe for northern summer 2003 (1 June – 31
123 August) to explore the impact of S-5P CO total column measurements on lowermost tropospheric air
124 pollution analyses, with a focus on CO PBL concentrations. The severe heat wave experienced in Europe
125 during northern summer 2003, and the concomitant atmospheric pollution and fire episodes, had a strongly
126 negative societal impact, being responsible for the deaths of over 14,000 people in France (Vautard et al.,
127 2005). This period had extremely hot and dry weather conditions and the long lasting atmospheric blocking
128 conditions significantly contributed to the accumulation of pollutants in the PBL owing to extended
129 residence time of the air parcels (Solberg et al., 2008). The spatial distribution of the enhanced levels of CO
130 and ozone was much more widespread over Europe during that summer than in previous ones (Lee et al.,
131 2006; Ordoñez et al., 2010). These exceptional weather conditions also resulted in several extreme wildfire
132 episodes over the Iberian Peninsula and the Mediterranean coast (Barbosa et al., 2004). Tressol et al. (2008)
133 point out that between 6 and 10 August 2003 the contribution of biomass burning to measured CO levels in
134 the lowermost troposphere reached 35% of the total CO field at these levels, a value comparable to typical
135 European anthropogenic emissions which represent 30% of this total CO field. Thus, the three-month period
136 1 June - 31 August 2003 includes both extreme and normal conditions, and provides an opportunity to study
137 the full range of pollution levels that occur in a summer season over Europe.
138
139 The OSSE study domain covers the larger part of Europe (5W-35E, 35N-70N), and we perform the OSSE
140 simulations at the spatial resolution of 0.2 degrees (latitude and longitude). This corresponds to a spatial
141 resolution of ~20 km (meridionally) and ~15 km (zonally, at 45N). With this spatial resolution, we can track
142 long-range transport plumes of CO. The length of the study period ensures we can sample different
143 meteorological situations typical for summertime, and provides an acceptable compromise between run-time
144 restrictions and provision of sufficient information for statistically significant results.
145
146 The structure of the paper is as follows. In Sect. 2 we describe the various components of the OSSE; in Sect.
147 3 we present the results from the OSSE for S-5P during summer 2003 over Europe. Finally, Sect. 4 provides
148 conclusions and identifies further work. A guiding principle in the OSSE set-up in this paper is to avoid
149 overoptimistic results.

Atmos. Chem. Phys. Discuss., doi:10.5194/acp-2015-924, 2016
Manuscript under review for journal Atmos. Chem. Phys.
Published: 1 February 2016

Atmospheric Chemistry and Physics Discussions

150

151 2. The OSSE set-up

152 The OSSE concept consists of simulating observations and their associated errors from a representation of
153 reality (the “Nature Run" or NR) and providing this information to a data assimilation system to produce
154 estimates of the NR states. Thereafter, one compares these estimates of the NR states from an assimilation
155 run, AR (where the observation of interest has been assimilated), and from a control run, CR (in this case a
156 free model run), against the NR. The performance of the AR and the CR against the NR quantifies the benefit
157 of the observation of interest.

158

159 The OSSEs are widely used in the meteorological community for assessing the usefulness of new
160 meteorological satellite data. Recent examples (not exhaustive) include the work of Lahoz et al. (2005),
161 Stoffelen et al. (2006), and Tan et al. (2007); Masutani et al. (2010a) reviews the OSSE methodology and
162 provides a comprehensive list of references of OSSEs for meteorological applications. By contrast, there are
163 relatively few studies concerning OSSEs for AQ applications (Edwards et al., 2009; Timmermans et al.,
164 2009a, b; Claeyman et al., 2011; Zoogman et al., 2011; 2014a, b; Yumimoto, 2013). In a recent review,
165 Timmermans et al. (2015) comment that documented AQ OSSEs have demonstrated the benefits that could
166 accrue from proposed and planned satellite platforms for AQ monitoring and forecasting. In the study
167 described in this paper, the set-ups for the NR, and the CR and AR, use different models, thereby avoiding
168 the identical twin problem typically associated with overly optimistic OSSE results (see, e.g., Masutani et al.,
169 2010a). In Sects. 2.1-2.5 we describe the various elements of the OSSE study described in this paper. Figure
170 1 in Timmermans et al. (2015) provides a schematic showing the relationships between the various elements
171 in an OSSE.

172

173 2.1 The Nature Run

174 A key element of an OSSE is the NR that defines the true state used to evaluate analyses and/or forecasts
175 using simulated observations. The NR commonly consists of a long, free-running forecast evolving
176 continuously in a dynamically consistent way (Masutani et al. 2010a, b). For this study, the basis of the NR
177 consists of two high-resolution free model simulations performed with: (i) the regional LOTOS-EUROS air

quality model (Schaap et al., 2008), and (ii) the global chemistry transport model TM5 (Huijnen et al., 2010). We obtain the NR by combining the LOTOS-EUROS CO profiles from the surface to 3.5 km with the TM5 CO profiles from 3.5 km to the top of the atmosphere (identified by the TM5 model top at 0.1 hPa). We use spatial interpolation to merge the values near the boundary between the two models at a height of 3.5 km. The model simulations used to construct the NR have a spin-up period of three months. We archive the NR output data on an hourly basis.

To construct the NR, we run the LOTOS-EUROS model at a horizontal resolution of about 7 km nested into the TM5 model, the latter run with a zoom domain over Europe at 1x1 degrees resolution. The TM5 model has 34 layers with a model top at 0.1 hPa. The LOTOS-EUROS model describes air pollution in the lowermost troposphere. It has four vertical layers following the dynamic mixing layer approach. The first layer is a fixed surface layer of 25 metres thickness, the second layer (boundary layer) follows the mixing layer height, and there are two reservoir layers spanning the rest of the atmosphere up to 3.5 km. The implicit assumption of the LOTOS-EUROS model is the presence of a well-mixed boundary layer, so constituent concentrations are constant up to the top of the Planetary Boundary Layer. The meteorological data used as input for the LOTOS-EUROS model come from the European Centre for Medium-Range Weather Forecasts (ECMWF). Prescription of surface anthropogenic emission is from the TNO-MACC-II emission database (Kuenen et al., 2014), and fire emissions are from the MACC global fire assimilation system (GFAS v1; Kaiser et al., 2012).

In the design of an OSSE, it is important to demonstrate that the NR exhibits the same statistical behaviour as the real atmosphere in every aspect relevant to the observing system under study (Masutani et al., 2010a, b). For the LOTOS-EUROS model used to build the lowermost levels of the NR, there is extensive verification by comparison with European data and by frequent participation in international model comparisons. This is the case for ozone and particulate matter (see Hass et al., 2003; Cuvelier et al., 2007; van Loon et al., 2007; Stern et al., 2008; Manders et al., 2009; Curier et al., 2012; Márecal et al., 2015). To evaluate the NR, we compare the surface CO data to available ground-based CO measurements over Europe during northern summer 2003 (1 June – 31 August). For this comparison, we use the ground-based stations from the Airbase database. We consider all types of ground-based stations from this database because of the

Atmos. Chem. Phys. Discuss., doi:10.5194/acp-2015-924, 2016
Manuscript under review for journal Atmos. Chem. Phys.
Published: 1 February 2016

limited number of available measurements, but we discard stations with less than 75% of hourly data within a month. This provides 171 ground-based stations for the comparison against the NR (note this approach results in a paucity of stations over France).

Figure 1 shows the location of the selected Airbase ground-based stations measuring CO over Europe during northern summer 2003 (top panel), and the time-series of CO concentrations during 1 June – 31 August 2003, measured by the selected Airbase ground-based stations and simulated by the NR and the CR (bottom panel). Note that most ground-based stations selected are located in polluted areas, where big emission sources of CO are present. We form the time-series from the ground-based stations by averaging spatially over all the sites. We form the NR time-series similarly, but interpolate the NR surface data to the station location. We do not add random observation errors to the NR time-series.

From Fig. 1, we see that, generally, the NR captures reasonably well the features of observed CO temporal variability during the three phases characterizing the summer of 2003: before, during and after the heat wave (the heat wave occurred on 31 July – 15 August). The correlation coefficient, ρ, between the ground-based data and NR time-series shown in the middle panel is 0.71. From this, we conclude that the NR has a realistic representation of the CO diurnal cycle. Note that CO concentration levels in the NR are slightly lower than observed ones. The bias of the NR with respect to observed CO concentrations fluctuates around -10 % on average during normal conditions and reaches -20% within the heat wave period. This means that the NR reproduces the surface concentrations with a negative bias (NR lower than ground-based stations) between 10 and 20%. Nonetheless, the simulated CO concentrations and those measured by the ground-based stations generally fall within the same range of values (between 200 and 400 μgm^{-3}). Thus, for the OSSE period considered, we conclude that the NR is representative of the variability of actual observations over the European domain, albeit with a negative bias.

Additionally, from Fig. 1 the behaviour of the CO time-series from the CR compared to the NR, is similar to the behaviour of the NR CO time-series compared to the Airbase data. This suggests that the configuration of our model is reasonably realistic, and reduces the likelihood that the OSSE produces overoptimistic results.

Atmos. Chem. Phys. Discuss., doi:10.5194/acp-2015-924, 2016
Manuscript under review for journal Atmos. Chem. Phys.
Published: 1 February 2016

2.2 The S-5P CO simulated measurements

The S-5P will deploy the TROPOspheric Monitoring Instrument (TROPOMI) jointly developed by The Netherlands and ESA (Veefkind et al. 2012). The TROPOMI instrument has heritage from both the OMI and the SCIAMACHY missions. The TROPOMI instrument will make measurements in the UV-visible wavelength range (270-500 nm), the near infrared, NIR (675-775 nm) and the shortwave infrared, SWIR (2305-2385 nm). It will deliver a key set of gas and aerosol data products for air quality and climate applications, including ozone, NO_2, formaldehyde, SO_2, methane and CO.

To enable sounding of the lower atmosphere at finer scales, TROPOMI has an unprecedented spatial resolution of 7x7 km^2 at nadir. This relatively high spatial resolution is necessary for air quality applications at local to regional scales. It will resolve emission sources with relatively high accuracy, and will obtain an acceptable fraction of cloud-free spectra. In contrast to the advantages provided by the relatively high spatial resolution of S-5P and design improvements, the SCIAMACHY CO data needs averaging in time (roughly one month) and space (5x5 degrees) to obtain realistic CO distributions at comparable uncertainty (Galli et al., 2012). Furthermore, TROPOMI will have a wide swath of 2600 km to allow for daily global coverage. The relatively high radiometric sensitivity of S-5P will allow measurements at low albedo, thus helping track smaller pollution events and improving the accuracy of air quality assessments and forecasts. The use of S-5P CO total column measurements with inverse modelling techniques will also help quantify more accurately biomass burning emissions and map their spatial distribution. The simultaneous measurements of CO and, e.g. NO_2, will provide additional information on wildfire and other pollution episodes (Veefkind et al., 2012).

The NR results were used to generate a set of synthetic S-5P observations. This involves several steps: 1) Generating realistic S-5P orbits and geolocation and viewing/solar geometries for the appropriate overpass time; 2) Using the ECMWF modelled cloud distributions to generate effective cloud fractions; 3) Generation of lookup tables for the averaging kernels and observation errors; 4) Collocation and application of the NR to derive a set of synthetic observations for 3 Summer months and 3 Winter months. These steps are discussed in the sub-sections below.

Atmos. Chem. Phys. Discuss., doi:10.5194/acp-2015-924, 2016
Manuscript under review for journal Atmos. Chem. Phys.
Published: 1 February 2016

Atmospheric Chemistry and Physics Discussions

2.2.1 Orbit simulator

The System Tool Kit (STK, available from AGI, http://www.agi.com/products/) is used to generate the S-5P orbit geometry and the geolocation of the edges of the swath as a function of time. Based on these characteristics, the location of the individual observations with a spatial distance of 7 km are generated. Time and longitude shifts are applied to the STK orbits to generate the orbits for the three Summer and three Winter months. Subsequently, the solar and viewing geometries are computed. Finally, segments of the orbits are maintained that have an overlap with the modelling domain.

2.2.2 Cloud properties

Cloud fields are obtained from the high-resolution operational weather forecast archive of the ECMWF. Meteorological fields of liquid water content, ice water content, specific humidity and cloud fraction are retrieved at a resolution of 0.25 x 0.25 degree for June-August 2003 and November 2003 - January 2004. These quantities are converted to cloud optical properties. The optical properties determine the reflectance, and are used to estimate effective cloud fractions and effective cloud top heights as would be retrieved from the satellite observations (Acarreta et al., 2004). The distribution of effective cloud fractions was compared with the distribution of effective cloud fractions obtained from OMI observations, and a reasonable agreement was found for Summer and Winter months.

These effective cloud fractions (and corresponding cloud radiance fractions) are used to provide weights to the cloud-free and cloud-covered fractions of the surface scene. The cloud altitude is used for the computation of the averaging kernel.

2.2.3 Averaging kernel and measurement uncertainty lookup tables

Because of the large number of observations that will become available from the S-5P instrument, full radiative transfer calculations for each observation separately is not feasible. We have chosen to build look-up tables for a set of geometries based on a radiative transfer code that employs the adding-doubling method in combination with optimal estimation (radiative transfer toolbox DISAMAR; de Haan, 2012). Look-up tables are set up for the averaging kernels (1D vectors as a function of altitude) and the measurement

uncertainty. Results are stored for a number of surface albedos, cloud/surface pressures, solar zenith angles, viewing zenith angles and relative azimuth angles. The look-up table details are provided in Table 1. Kernels are provided on 21 pressure levels between 1050.0 and 0.1 hPa. Uncertainties are specified for clear-sky and cloudy-sky separately.

Each simulation with DISAMAR consist of a forward calculation of the satellite-observed spectrum, followed by a retrieval step based on the optimal estimation method (Rodgers, 2000). Instrument noise, listed in Table 1, is converted into uncertainties for the retrieved CO column. A-priori trace gas profiles are taken from the CAMELOT study (Levelt et al., 2009). We assume that both the cloud and the surface are Lambertian reflectors. Kujanpää et al. (2015) provide further details of this procedure.

In particular the albedo is of major influence for the uncertainty, because it directly determines the signal observed by the instrument. This dependence is shown in Fig.2. Over land, albedo values are typically of the order of 0.1-0.2, with typical column errors of the order of 2 DU, or about 10^{17} molecules cm^{-2}. Because typical CO columns over Europe are 2 10^{18} molecules cm^{-2}, this is a relatively small error of the order of 5%. These numbers are in good agreement with the results presented in the CO ATBD of TROPOMI (document expected to be publicly released by the end of 2015). Over Sea, the albedo is very low, and the noise dominates the signal. In order to simulate this behaviour in a realistic way we have added the albedo values 0.005, 0.01 and 0.02 to the albedo list.

We note that the uncertainties reported here are substantially lower than those reported for SCIAMACHY (e.g. Gloudemans et al., 2008). This reflects a difference in specifications of the instruments, and the fact that SCIAMACHY observations were hindered by ice build-up on the detectors. Real TROPOMI observations will show if the relatively small errors are realistic.

2.2.4 Synthetic observations generation

The generation of the synthetic observations consists of the following steps:

- Collocation of the Nature run vertical profiles of CO to the locations of the observations.

Atmos. Chem. Phys. Discuss., doi:10.5194/acp-2015-924, 2016
Manuscript under review for journal Atmos. Chem. Phys.
Published: 1 February 2016

- Computation of the effective cloud fraction, cloud radiance fraction, and cloud pressure from the ECMWF cloud fields collocated to the observations.
- Collocation of the NIR albedo map (Surface albedo at 2300 nm is interpolated from a climatology provided by SRON and based on SCIAMACHY observations (P. Tol, personal communication)) to the locations of the observations.
- Extract interpolated values for the observation kernel and uncertainties from the look-up table.
- Compute the synthetic observation from the inner product of the kernel with the nature run CO profile. This is done for both a clear sky and fully clouded situation, using the cloud pressure.
- Add a random noise amount to each observation, by drawing numbers from a Gaussian distribution with a width determined from the uncertainty estimate.
- Compute the partially clouded synthetic observation by weighting the clear and cloudy results with the cloud radiance fraction.

Over land, and in clear sky cases, the averaging kernel is close to 1, showing that the S-5P instrument is observing the vertical column to a good approximation (see Fig. 3). In cloud-covered cases the kernel equals 0 for layers below the cloud pressure (yellow line in Fig. 3). For low-albedo cases (over ocean), Rayleigh scattering becomes non-negligible, and the kernel is decreasing towards the surface, but the noise is dominant in this case.

The results of this process is shown in Fig. 4. The figure demonstrates the high resolution of the NR (about 7 km) and the corresponding simulated amount of detail. The bottom panel shows the corresponding CO observations. Over land the NR features are clearly present due to the relatively low uncertainty. Over the ocean and Mediterranean the signal is dominated by the noise. An improved information content is observed near Iceland, related to a thick cloud cover, where the higher signal reduces the relative noise.

2.3 Pre-processing of S-5P CO total column observations

This section describes the pre-processing of S-5P CO total column observations prior to assimilation into the MOCAGE model (Peuch et al., 1999) for the OSSE simulations. Using the MOCAGE model for the AR and

Atmos. Chem. Phys. Discuss., doi:10.5194/acp-2015-924, 2016
Manuscript under review for journal Atmos. Chem. Phys.
Published: 1 February 2016

348 CR simulations avoids the identical twin problem associated with using the same model for both the NR and
349 the OSSE simulations, which typically produces overoptimistic results (Arnold and Dey, 1986; Stoffelen et
350 al., 2006). Section 2.4 provides further details of the MOCAGE model.
351
352 The S-5P will produce large amounts of data owing to its wide swath and relatively high spatial resolution of
353 about 7x7 km^2. Thus, a pre-processing step is necessary to reduce the data volume for the data assimilation
354 experiments. For this study, we consider only pixels inside the OSSE simulation domain (Note that retrieval
355 pixels in each single cross-track are essentially instantaneous measurements of CO.). This has the advantage
356 of alleviating the data volume burden. However, a single cross-track over Europe could have more than
357 80,000 valid retrieval pixels. Furthermore, each individual pixel is associated with an averaging kernel vector
358 given at 34 vertical pressure levels, from the surface up to the top of the atmosphere (identified as 0.1 hPa).
359
360 Figure 3 shows an example of averaging kernels at the surface, as well as the averaging kernels
361 representative of retrievals including pixels with different cloud fractions (less than 10%, greater than 30%,
362 and greater than 80%). In addition, we discard data points with solar zenith angles larger than 80% or errors
363 exceeding 20%. The retrieval over sea is noise-dominated. Because of this, we only consider CO partial
364 columns above cloudy sea scenes with cloud fraction more than 80% and cloud top heights between the
365 surface and 650 hPa. Finally, we apply a spatially weighted mean to bin the measurements into 0.2° x 0.2°
366 grid boxes (~20 x 15 km at 45N), the assimilation model resolution; this is the set-up used for the OSSE
367 assimilation experiments (CR and AR), and is described in El Amraoui et al. (2008a). It combines the
368 MOCAGE model and the PALM (Projet d'Assimilation par Logiciel Multiméthode) data assimilation
369 module. Sections 2.4-2.5 provide further details of the CR and AR set-ups.
370
371 The weighted mean for pixels falling in the same model grid box is:
372

$$\bar{c} = \frac{\sum_i w_i c_i}{\sum_i w_i}$$

373
374

Atmos. Chem. Phys. Discuss., doi:10.5194/acp-2015-924, 2016
Manuscript under review for journal Atmos. Chem. Phys.
Published: 1 February 2016

Atmospheric Chemistry and Physics Discussions

375 where $\bar{c}$ is the weighted average, c_i a single column measurement, and w_i ($=1/\sigma_i^2$) is the inverse of the
376 variance corresponding to measurement c_i, and is the weight assigned to this single measurement. The
377 inverse of the variance associated with the weighted average is
378

$$\frac{1}{\bar{\sigma}^2} = \sum_i w_i$$

379
380

381 The spatial binning not only reduces considerably the data volume but also results in an improved spatial
382 representativeness of the CO measurements by reducing the random error of each data pixel.
383

384 **2.4 The Control Run**

385 To generate the CR, it is important to use a state-of-the-art modelling system, which simulates the
386 observational data representing, for example, a current operational observational system. An important
387 requirement for an effective OSSE is to generate the CR with a model different to the one used to construct
388 the NR to avoid the identical twin problem (see Sect. 2.3). If the model from which we extract hypothetical
389 observations is the same as the assimilating model, the OSSE results tend to show unrealistic observation
390 impact and overly optimistic forecast skill (Arnold and Dey, 1986; Stoffelen et al., 2006). Consequently, by
391 using two independent models the OSSE will more realistically simulate the assimilation of real
392 observations. This follows our guiding principle to design an OSSE that is not too overoptimistic.
393

394 As mentioned in Sect. 2.3, we use the MOCAGE model to generate the CR. In this OSSE study, the CR is a
395 free model run. The MOCAGE model is a three-dimensional CTM developed at Météo France (Peuch et al.,
396 1999) providing the evolution of the atmospheric composition in accordance with dynamical, physical and
397 chemical processes. It provides a number of configurations with different domains and grid resolutions, as
398 well as various chemical and physical parameterization packages. Current use of MOCAGE includes several
399 applications: e.g., the Météo-France operational chemical weather forecasts (Dufour et al., 2004); the
400 Monitoring Atmospheric Composition and Climate (MACC) services (http://www.gmes-atmosphere.eu;
401 Márecal et al., 2015); and studies of climate trends of atmospheric composition (Teyssèdre et al., 2007).

Atmos. Chem. Phys. Discuss., doi:10.5194/acp-2015-924, 2016
Manuscript under review for journal Atmos. Chem. Phys.
Published: 1 February 2016

Validation of MOCAGE simulations against a large number of measurements took place during the Intercontinental Transport of Ozone and Precursors (ICARTT/ITOP) campaign (Bousserez et al., 2007).

In this study, we use a two-way nesting configuration to generate the CR and the AR (we describe the AR set-up in Sect. 2.5): a global grid with a horizontal resolution of 2x2 degrees and a regional grid (5W-35E, 35N-70N) with a horizontal resolution of 0.2x0.2 degrees. The MOCAGE model includes 47 sigma-hybrid vertical levels from the surface up to 5 hPa. The vertical resolution is 40 to 400 m in the boundary layer (7 levels) and about 800 m in the neighbourhood of the tropopause and in the lower stratosphere. The chemical scheme used is RACMOBUS, which combines the stratospheric scheme REPROBUS (Lefèvre et al., 1994) and the tropospheric scheme RACM (Stockwell et al., 1997). The RACMOBUS scheme includes 119 individual species, of which 89 are prognostic variables, and considers 372 chemical reactions.

We force the CR (and the AR) every 3 hours with the ARPEGE analysis (Courtier et al., 1991). We prescribe the surface anthropogenic emission using the MACC-I emission database (https://gmes-atmosphere.eu/about/project_structure/input_data/d_emis/). We do not include the fire emissions in the CR and AR experiments described in this paper, as they are a priori not known. This means that any signature of fire emissions in the AR (see Sect. 2.5) can only come from assimilation of the CO measurements. Note that for the NR, the surface anthropogenic emissions come from the MACC-II inventory, helping to differentiate the CR from the NR. As for the NR, the CR has a spin-up period of three months.

2.5 The Assimilation run

We assimilate simulated S-5P total column CO observations derived from the LOTOS-EUROS NR into the MOCAGE CTM at a 0.2° spatial resolution using the MACC extended domain (5W-35E, 35N-70N). The assimilation system used in this study is MOCAGE-PALM (e.g., El Amraoui et al., 2008a) developed jointly by Météo-France and CERFACS (Centre Européen de Recherche et de Formation Avancée en Calcul Scientifique) in the framework of the ASSET European project (Lahoz et al., 2007b). The assimilation module used in this study is PALM, a modular and flexible software, which consists of elementary components that exchange data (Lagarde et al., 2001). It manages the dynamic launching of the coupled

Atmos. Chem. Phys. Discuss., doi:10.5194/acp-2015-924, 2016
Manuscript under review for journal Atmos. Chem. Phys.
Published: 1 February 2016

components (forecast model, algebra operators and input/output of observational data) and the parallel data exchanges. Massart et al. (2009) used the assimilation system MOCAGE-PALM to assess the quality of satellite ozone measurements. The MOCAGE-PALM assimilation system also helps identify and overcome model deficiencies. In this context, its assimilation product has been used in many atmospheric studies in relation to ozone loss in the Arctic vortex (El Amraoui et al., 2008a); tropics/mid-latitudes exchange (Bencherif et al., 2007); stratosphere-troposphere exchange (Semane et al., 2007); and exchange between the polar vortex and mid-latitudes (El Amraoui et al., 2008b). For this OSSE, to speed up the assimilation process we use the 3D-Var version of PALM. In the OSSE, the MOCAGE model provides the CR and by assimilating the simulated CO data from the NR, the MOCAGE model provides the AR. Thus, we produce the CR and AR outputs with a model different from that used to produce the NR (see Sect. 2.1).

A key element of the data assimilation system is the background error covariance matrix (the **B**-matrix) (Bannister, 2008). It has a large impact on the 3D-Var analysis used in this study and, thus, it is important to use a form of **B** that is as realistic as possible. In MOCAGE-PALM, we base the **B**-matrix formulation on the diffusion equation approach (Weaver and Courtier, 2001). It can be fully specified by means of the 3-D standard deviation field (square root of the diagonal elements of **B**, in concentration units or as a percentage of the background field) and 3-D fields of the horizontal (L_x and L_y) and vertical (L_z) local correlation length-scales. We can estimate the **B**-matrix elements more efficiently using an ensemble method (Bannister, 2008). This technique consists of feeding an ensemble of states through the data assimilation system to simulate the important sources of error. However, this approach is time-consuming and, therefore, not used in this study.

For this study, we use a simple parameterization for the **B**-matrix: L_x and L_y are assumed homogeneous and equal to 35 km (about two model grid lengths); L_z is constant and set to one vertical model layer. As in Emili et al. (2014), the background standard deviation 3-D field is parameterized as a vertically varying percentage of the background profile, which decreases from values of 25% at the surface to values of 15% in the upper troposphere, and decreases further throughout the stratosphere to values of 5% in the upper stratosphere (not shown). We base these settings on several 1-day assimilation trials; they ensure reasonable values of standard self-consistency tests, e.g., providing chi-squared (χ^2) values close to 1 (see Fig. 3 in Sect. 3.1). Furthermore,

Atmos. Chem. Phys. Discuss., doi:10.5194/acp-2015-924, 2016
Manuscript under review for journal Atmos. Chem. Phys.
Published: 1 February 2016

a value of L_x and L_y of 35 km corresponds to more than one grid length of the model, allowing the model to resolve these features. The data assimilation procedure will weight both the observations and the model 1-hour forecasts (from the last analysis point), and will update locations not coincident with the observations through the correlation length-scales. Table 2 summarizes the parameters used for the assimilation experiments.

3. Results

3.1 Evaluation of the assimilation run

In this section, we evaluate the impact of the assimilation of the S-5P CO total column. First, we evaluate the consistency of the assimilation run by separating the clear-sky pixels from their cloudy counterparts (Sect. 3.1.1). Second, to further understand the impact on the surface CO field of the simulated S-5P CO total column measurements, we investigate the analysis increment (δx) to provide a quantitative diagnostic of the quality of the analysis for a selected date, 15 June 2003 (Sect. 3.1.2).

3.1.1 Consistency of the assimilation run

We have performed two OSSEs. The first one includes all pixels in the OSSE domain, regardless of whether they are cloudy or clear-sky and the second only includes clear-sky pixels. A pixel is considered as clear when the cloud fraction is less than 10%. Comparison of the ARs from these two OSSEs indicated that the impact of including all pixels is small. The largest differences between the respective ARs in relation to the NR are 4% in regions over North Europe (North Sea and Scandinavia), with the AR for clear-sky pixels closer to the NR (not shown). We can explain these results by the fact the summer generally has low amounts of cloud. Consequently, we only present the results from the OSSE with all pixels.

To evaluate the AR, we calculate the χ^2 diagnostic associated with the Observation minus Forecast (OmF) differences (see, e.g., Lahoz et al., 2007a). Here, we normalize the OmF differences by the background error. We also calculate histograms of the Observation minus Analysis (OmA) differences, the observation and the simulation from the CR (observation-minus-control run, hereafter OmC) differences, and the OmF

Atmos. Chem. Phys. Discuss., doi:10.5194/acp-2015-924, 2016
Manuscript under review for journal Atmos. Chem. Phys.
Published: 1 February 2016

Atmospheric Chemistry and Physics Discussions

differences. We use the observational error to normalize the differences building the histograms of OmA, OmC and OmF.

Figure 5 (top panel) shows the chi-squared time-series for OmF and its associated auto-correlation function calculated over the three-month period of the OSSE experiments, computed as daily averages. The chi-squared diagnostic starts with a maximum of about 1.56, and takes values down to 0.75, with a mean of 0.9 over the OSSE three-month period. The chi-squared time-series is nearly stable since it exhibits relatively small variability (a standard deviation of about 0.14). Furthermore, the auto-correlation of the chi-squared statistic drops to zero, with no correlation after a time delay of 20 days. The calculation of the auto-correlation shows that the chi-squared statistic is uncorrelated after a time lag of 20 days; this means that after this time the mathematical expectation $E(\chi^2)$ is equal to the average of the chi-squared statistics. We find $E(\chi^2) = 0.90$, which is close to the theoretical value of 1 (see Lahoz et al., 2007a). This result indicates that the a priori error statistics as represented in the **B**-matrix slightly overestimate the actual error statistics from the OmF differences.

To test whether the observations, forecast and analysis fields, and their associated errors, are consistent with each other, we calculate the histograms of OmA, OmF and OmC only over land (normalized by the observation error) over the three-month period (Fig. 5, bottom panel). For a properly set up assimilation system, the OmF and OmA normalized histograms should be close to a Gaussian distribution with mean zero and standard deviation one. Figure 3 (bottom panel) shows that the OmA and OmF differences are close to a Gaussian distribution centred near to or at zero. The OmF has a mean and standard deviation of 0.10 and 1.73, respectively, whereas the OmA has nearly a zero mean and a standard deviation of 1.05. This indicates that the centre of the OmA histogram is closer to zero and more peaked than the histogram of OmF. We expect this, since the analyses should be closer to the observations than the forecasts. Furthermore, the histogram for OmA indicates that the errors in the **R**-matrix, the observational counterpart of the **B**-matrix, are a good representation of the analysis error.

Based on the above results, we conclude that the background error covariance matrix, **B**, and its observational counterpart, **R**, prescribed in our assimilation system are reasonably well characterized (see,

Atmos. Chem. Phys. Discuss., doi:10.5194/acp-2015-924, 2016
Manuscript under review for journal Atmos. Chem. Phys.
Published: 1 February 2016

514 e.g., Lahoz et al., 2007a, for a discussion of the specification of errors in a data assimilation system).
515 Furthermore, the above results are consistent with the assumption that the errors in the observations and the
516 forecasts are Gaussian.
517
518 The shape of the OmC normalized histogram, which has a mean and standard deviation of 2.36 and 5.60,
519 respectively, indicates the presence of a relatively large bias between the S-5P observations and the CR. The
520 assimilation reduces this bias, as shown by the analyses being significantly closer to the observations than
521 the simulation from the CR. This shows that the assimilation of simulated S-5P CO total column
522 observations has a significant impact on the CO forecasts and analyses.
523
524 ***3.1.2 Study of increments***
525 To understand further the impact on the surface CO field of the simulated S-5P CO total column
526 measurements, we calculate the analysis increment (δx) for a single analysis time at 14:00 UTC on 15 June
527 2003. We calculate this increment as the analysis minus the model first guess (1-hour forecast). The analysis
528 increment provides a quantitative diagnostic of the quality of the analysis (see, e.g., Fitzmaurice and Bras,
529 2008).
530
531 Figure 6 (top panel) shows the spatial distribution of δx at the model surface. One can see the spread of the
532 impact of the simulated observations across large regions. This is owing to S-5P having a wide swath
533 allowing it to sample larger regions. The most substantial corrections are over land, where there are sufficient
534 observations to have an impact. Over sea, the increments tend to be negligible, as any observations found
535 there have relatively large errors. Thus, there will not be much difference between the model first guess and
536 the analysis. Likewise, this is also true in the regions outside the satellite footprint.
537
538 To provide further insight into the impact of S-5P CO measurements, we calculate latitude-height and
539 longitude-height cross-sections at 48.8N, 2.6E, near Paris, for 15 June 2003. Figure 4 (bottom left and
540 bottom right panels) shows a zoom of the zonal and meridional vertical slices of the analysis increment. We
541 see significant corrections to the model first guess (identified by large increments) confined to a deep layer.
542 These corrections are larger at the surface, and exhibit a second maximum around 650 hPa. This vertical

Atmos. Chem. Phys. Discuss., doi:10.5194/acp-2015-924, 2016
Manuscript under review for journal Atmos. Chem. Phys.
Published: 1 February 2016

structure is mainly attributable to the forecast error standard deviation (given as a vertically varying fraction of the local CO mixing ratio), the square root of the diagonal entry of the **B**-matrix, and which is higher in the boundary layer (where the value of the S-5P CO averaging kernel is close to 1). The shape of the S-5P analysis increments also exhibits a second peak around 650 hPa. The increments for this particular day thus show a clear impact from the S-5P CO measurements in the PBL and the free troposphere.

The shape of the S-5P increments is similar to that of typical SCIAMACHY analysis increments, which also extend through a deep layer and have a maximum at the surface (Tangborn et al., 2009). The fact that both these analysis increments stretch out over a deep layer is owing to similarities in the S-5P and SCIAMACHY averaging kernels - both are close to unity over cloud-free land (see Fig. 4). Note that the situation shown in Fig. 6 is a snapshot and depends on the particular conditions for this time. An average of the increments over the summer period would tend to show a uniform distribution in height.

3.2 Evaluation of the summer OSSE

3.2.1 Summer averages

Figure 7 shows the fields of surface CO from the CR, and the NR and the AR, averaged over the northern summer period. One can see the general change of CO over land between the CR (top left panel) and the AR (bottom panel). We can ascribe this to the contribution of simulated S-5P total column CO data sampled from the NR. This figure shows several differences between the CR and AR fields that indicate the superior behaviour of the AR in capturing features in the NR. For example, over Eastern Europe and Russia, the AR CO concentration values are closer to those in the NR; in particular, the CR shows generally lower values than in the NR. Nevertheless, over Portugal, where the NR shows the forest fires that occurred over the summer, the AR captures them only slightly better than the CR. We expect the relatively poor performance of the CR regarding fires, as the fires are not included in the CR set-up (see Sect. 2.4). Although the AR captures the forest fires slightly better than the CR (through assimilation of CO measurements), the relatively poor temporal resolution of the S-5P ultimately limits its performance. A geostationary satellite, given its relatively high temporal resolution, should be able to capture better the temporal variability of these forest fires (Edwards et al., 2009).

Atmos. Chem. Phys. Discuss., doi:10.5194/acp-2015-924, 2016
Manuscript under review for journal Atmos. Chem. Phys.
Published: 1 February 2016

Atmospheric Chemistry and Physics Discussions

572 ***3.2.2 Statistical metrics***

573 In this section, we provide a quantitative assessment of the benefit from S-5P CO total column measurements
574 on the CO surface analysis. For this, we perform a statistical analysis of the different OSSE experiments for
575 northern summer 2003.

576

577 We calculate the mean bias (MB, in parts per billion by volume, ppbv), its magnitude reduction (MBMR,
578 ppbv), and the root mean square error (RMSE, ppbv), and its reduction rate (RMSERR, %). Note that
579 although recent papers have raised concerns over the use of the RMSE metric (Willmott and Matsuura, 2005;
580 Willmott et al., 2009), Chai and Draxler (2014) discuss circumstances where the RMSE is more beneficial.
581 We use the correlation coefficient, ρ to measure the linear dependence between two datasets, and the fraction
582 of the true variability (i.e., variability represented by the NR) reproduced by the CR or AR.

583

584 For a single model grid box, we define the statistical metrics (MB, RMSE, ρ) with respect to the NR as:

585

586 $$MB(X) = \frac{1}{N}\sum(X - NR)$$

587

588 $$MBMR = |MB(CR)| - |MB(AR)|$$

589

590 $$RMSE(X) = \sqrt{\frac{1}{N}\sum(X - NR)^2}$$

591

592 $$RMSERR = 100 \times \left(1 - \frac{RMSE(AR)}{RMSE(CR)}\right)$$

593

594 $$\rho(X) = \frac{\sum(X-\overline{X})(NR-\overline{NR})}{\sqrt{\sum(X-\overline{X})^2\sum(NR-\overline{NR})^2}}$$

595

Atmos. Chem. Phys. Discuss., doi:10.5194/acp-2015-924, 2016
Manuscript under review for journal Atmos. Chem. Phys.
Published: 1 February 2016

where X denotes the CR or the AR; N is the number of data samples; the vertical bars denote the absolute value operator; and the overbar symbol represents the arithmetic mean operator. The MB metric gives the average value by which the CR or the AR differs from the NR over the entire dataset.

3.2.3 Results of the statistical tests

Figure 8 presents the zonal and meridional means of the difference between the CR and the AR averaged over the northern summer 2003 (1 June – 31 August). We also plot the confidence interval representing the areas where the AR is not significantly different to the CR at the 99% confidence limit (highlighted in the grey colour). These two figures show that there is benefit from the S-5P CO total column data over the first few bottom levels of the troposphere, i.e., the lowermost troposphere. Between the surface and 800 hPa, a negative peak is present in the zonal difference field (over Scandinavia), and in the meridional difference field (over Eastern Europe). Note that the zonal field shows two areas, one with positive values and the other with negative values representing a CR greater than the AR and a CR smaller than the AR, respectively. The positive peak, at a slightly higher level (i.e., lower pressure) than the negative peak, is representative of the Mediterranean Sea, whereas the negative peak is more representative of the land areas (Scandinavia and Eastern Europe). Figure 8 indicates that the S-5P CO corrects the model in the lower troposphere with a larger impact over land and with a less large impact in the PBL. This is consistent with the behaviour of the analysis increments shown in Fig. 6.

Figure 9 shows the performance of the biases between the CR and the NR, and the AR and the NR at the surface, and averaged over the northern summer of 2003 (1 June – 31 August). The MBMR, which compares the magnitude of the CR vs NR and AR vs NR biases, indicates the geographical areas where the simulated S5P CO total column data have the most impact. The MBMR shows that the AR is closer to the NR than the CR, almost everywhere in the domain (reflected by the prevalence of the red colours in the bottom left panel). This indicates that the simulated S-5P CO total column data generally provide a benefit at the surface, and especially over land areas where the CO sources are sparse.

We also calculate the RMSE as well as the reduction rate of the RMSE, RMSERR (Figure 10), both keeping the systematic error (Fig. 10 top), and removing the systematic error (Fig. 10 bottom). We calculate the

625 systematic error in the AR and CR by subtracting the NR field from each of them, producing a debiased AR
626 and CR. For the case where we remove the systematic error, we perform the statistics on the debiased AR
627 and CR. If we examine the RMSE statistics, Fig. 8 shows that the CR gets closer to the NR over the Atlantic
628 Ocean and over the Eastern domain including Russia and Scandinavia, when we remove the systematic error.
629 For example, over these areas we obtain ~30 ppbv and ~10 ppbv for the RMSE keeping and removing the
630 systematic error, respectively. For the reduction of the RMSE, RMSERR, the behaviour for the CR is similar
631 overall, showing a reduction rate of 60% and 30-45% keeping and removing the systematic error,
632 respectively. Note that over Scandinavia the reduction rate goes down from 60% to about 10% after
633 removing the systematic error.
634
635 These results indicate that S-5P CO data show more benefit when keeping the systematic error in the
636 calculation of the RMSE. Following our guiding principle of avoiding an overoptimistic OSSE, we consider
637 only the values of RMSE obtained when we remove the systematic error. For this case, the average reduction
638 rate for the AR is around 20-25% over land (except Scandinavia) and close to 10% over sea and over
639 Scandinavia.
640
641 In Figure 11, we show the correlation between the CR and the NR, and the correlation between the AR and
642 the NR, at the surface for the three northern summer months (1 June – 31 August). Figure 11 shows that the
643 AR is closer than the CR to the NR with the correlation coefficient reaching 0.9 over land. By contrast, the
644 correlation coefficient between the CR and the NR is typically less than 0.5, with very low values over
645 Eastern Europe, where CO sources are sparse.
646
647 ***3.2.4 Time-series at selected locations***
648 Figure 12 shows time-series from the NR, the CR and the AR over the three areas of the study domain
649 represented by the squares shown in Figs. 9 (bottom panel) and 10 (right panels). (i) The Paris region (Fig.
650 12, top panel); (ii) a region over Portugal, where forest fires occurred during the northern summer (Fig. 12,
651 middle panel); and (iii) an area in the Eastern part of the study domain, where the reduction of RMSE (i.e.,
652 RMSERR) was much larger than for other regions (Fig. 12, bottom panel). For all three areas, the AR is
653 generally closer to the NR than the CR, showing the impact of the simulated observations. We calculate the

Atmos. Chem. Phys. Discuss., doi:10.5194/acp-2015-924, 2016
Manuscript under review for journal Atmos. Chem. Phys.
Published: 1 February 2016

biases between the AR and CR vs the NR by computing the difference NR-X, where X is AR or CR, and normalizing by the number of observations over the northern summer period. The biases are: (i) Paris region, CR: 48 ppbv, AR: 38 ppbv; (ii) Portugal, CR: 101 ppbv, AR: 83 ppbv; (iii) Eastern part of domain: CR: 21 ppbv, AR: 5 ppbv.

Over Paris (top panel), the CR is already close to the NR and the impact of the S-5P CO simulated observations is small. Over Portugal (middle panel), the presence of fires is not seen in the CR (e.g., a maximum of CO at the beginning of the heat wave), as the fires were not taken into account in the CR as they are not known a priori (see Sect. 2.4). In contrast, over this specific location we see the impact of the fires on the CO concentrations in the AR with, however, much lower values than for the NR. During the fires, the CO concentrations in the AR over Portugal were larger than 500 ppbv, whereas the CR remained relatively unchanged with concentrations less than 200 ppbv. Over the Eastern part of the study area (bottom panel), the temporal variability is not high and the magnitude of the bias between the CR and the NR is small, but it is removed in the AR.

3.2.5 Sensitivity tests for fire episode

The assimilation system we use has a default criterion to discard CO column observations with values larger than 75% of the MOCAGE value. This criterion is not appropriate to situations resulting in excessive values in the CO concentrations, as is the case for forest fires. To understand further the performance of the OSSE over the period of the Portugal forest fires we perform a second OSSE without this default criterion. This second OSSE covers the period of the forest fires (25 July – 15 August). For this second OSSE, we compare the total column values and the surface values of the CO fields from the CR and the AR (Figs. 13-15, respectively).

Figure 13 shows the CO total column at 14:15 UTC on 4 August 2003 (during the period of the Portugal forest fires) from the NR (top left panel); the simulated S-5P observations (top right panel); the CR (bottom left panel); and the AR (bottom right panel). We can see that the AR captures the fire event, indicated by relatively high values of the CO total column over Portugal, whereas the CR does not. This confirms the results shown in Fig. 12, which highlight the benefit provided by the S-5P CO total column measurements, in

particular regarding the capture of the signature of the Portugal forest fires. Note that the S-5P measurement is noise-dominated over the sea (top right panel). This accounts for the sharp edge in the CO total column field seen between the Iberian Peninsula and the Bay of Biscay for the AR (bottom right panel).

Figure 14 shows the time-series of the surface CO concentrations over the period 25 July – 15 August (that of the Portugal forest fires). In comparison to the original OSSE (see middle panel of Fig. 12), the AR is now closer to the NR, having now peak values of about 900 ppbv, instead of peak values of about 550 ppbv. The CR still has peak values less than 200 ppbv. This indicates that the relatively low values in the AR (in comparison to the NR) for the original OSSE shown in the middle panel of Fig. 12 result from the application of the default criterion to discard CO column observations that are far away from MOCAGE values. The results from Fig. 14 confirm those shown in Fig. 13, and reinforce the benefit provided by the S-5P CO total column measurements, in particular regarding the capture of the signature of the Portugal forest fires.

4. Conclusions

We perform a regional-scale Observing System Simulation Experiment (OSSE) over Europe to explore the impact of the LEO satellite mission S-5P carbon monoxide (CO) total column measurements on lowermost tropospheric air pollution analyses, with a focus on CO surface concentrations and the Planetary Boundary Layer (PBL). The PBL varies in depth throughout the year, but is contained within the lowermost troposphere (heights 0-3 km), and typically spans the heights 0-1 km. We focus on northern summer 2003, which experienced a severe heat wave with severe societal impact.

This OSSE study provides insight on the impact from LEO S-5P CO measurements on surface CO information. We perform the standard steps of an OSSE for air quality. (i) Production of a Nature Run, NR. (ii) Test of the realism of the NR. (iii) Different models to produce, on the one hand, the NR, and on the other hand, the OSSE experiments to create the Control Run, CR, and the Assimilation Run, AR. (iv) Calculation of synthetic observations, observation uncertainty, and averaging kernels to represent sensitivity of the observations in the vertical. (v) Quantitative evaluation of the OSSE results, including performing statistical

711 significance tests, and self-consistency and chi-squared tests. Based on the specifications of the TROPOMI
712 instrument, relatively low CO column uncertainties of around 5% are anticipated over the European
713 continent.
714
715 Our guiding principle in the set-up of this OSSE study is to avoid overoptimistic results. To achieve this, we
716 address several factors considered likely to contribute to an overoptimistic OSSE. (i) We use different
717 models for the NR and the OSSE experiments. (ii) We check that the differences between the NR and actual
718 measurements of CO are comparable to the CO field differences between the model used for the OSSE and
719 the NR. (iii) We remove the systematic error (calculated as the bias against the NR) in the OSSE outputs (AR
720 and CR) and compare the debiased results to the NR.
721
722 The OSSE results indicate that simulated S-5P CO total column measurements during northern summer 2003
723 benefit efforts to monitor surface CO. The largest benefit occurs over land in remote regions (Eastern
724 Europe, including Russia) where CO sources are sparse. Over these land areas, and for the case when we
725 remove the systematic error, we obtain a lower RMSE value (by ~10 ppbv) for the AR than for the CR, in
726 both cases vs the NR. Over sea and Scandinavia, we also obtain a lower RMSE (by ~10%) for the AR than
727 for the CR, in both cases vs the NR. Consistent with this behaviour, we find the AR is generally closer to the
728 NR than the CR to the NR, with a correlation coefficient reaching 0.9 over land (NR vs AR). By contrast, the
729 correlation coefficient between the CR and the NR is typically less than 0.5, with very low values over
730 Eastern Europe, where CO sources are sparse. In general, for all the metrics calculated in this paper, there is
731 an overall benefit over land from the S-5P CO total column measurements. Significance tests on the CR and
732 AR results indicate that, generally, the differences in their performance are significant at the 99% confidence
733 level. This indicates that the S-5P CO total column measurements provide a significant benefit to monitor
734 surface CO.
735
736 We further show that, locally, the AR is capable of reproducing the peak in the CO distribution at the surface
737 due to forest fires (albeit, weaker than the NR signal), even if the CR does not have the signature of the fires
738 in its emission inventory. A second OSSE shows that this relatively weak signal of the forest fires in the AR
739 arises from the use of a default criterion to discard CO total column observations too far from model values,

740 a criterion not appropriate to situations resulting in excessive values in the CO concentrations, as is the case
741 for forest fires. This second OSSE shows a much stronger signal in the AR, which is now much closer to the
742 NR than the CR, confirming the benefit of S-5P CO total column measurements.
743
744 Further work will involve extending the OSSE approach to other S-5P measurements, such as ozone total
745 column, and NO_2 and formaldehyde tropospheric columns. These studies will complement similar studies on
746 the benefit from Sentinel-4 and -5 measurements. Collectively, these OSSE studies will provide insight into
747 the relative benefits from the Sentinel-4, -5 and -5P platforms for monitoring atmospheric pollution
748 processes.
749

750 ## 5. Acknowledgments

751 Support for this work came partly from the ESA funded project “Impact of Spaceborne Observations on
752 Tropospheric Composition Analysis and Forecast” (ISOTROP –ESA contract number 4000105743). WAL
753 acknowledges support from an internal project from NILU. RA, JLA, PR, LE and WAL acknowledge
754 support from the RTRA/STAE. JK and JT acknowledge support from the Academy of Finland (Project no.
755 267442).
756

6. References

Acarreta, J. R., J. F. De Haan, and P. Stammes (2004), Cloud pressure retrieval using the O2-O2 absorption band at 477 nm, J. Geophys. Res., 109, D05204, doi:10.1029/2003JD003915.

Arnold, C.P., Jr., and C.H. Dey, 1986: Observing-systems simulation experiments: Past, present and future. Bull. Amer. Meteorol. Soc., 67, 687–695.

Atlas, R. 1997: Atmospheric observation and experiments to assess their usefulness in data assimilation. J. Meteor. Soc. Jpn., 75, 111–130.

Atlas, R., G.D. Emmitt, Terry, E. Brin, J. Ardizzone, J.C. Jusem, et al., 2003: Recent observing system simulation experiments at the NASA DAO, in Preprints, 7th Symposium on Integrated Observing Systems (Long Beach, CA: American Meteorological Society).

Bannister, R.N., 2008: A review of forecast error covariance statistics in atmospheric variational data assimilation. I: characteristics and measurements of forecast error covariances. Q. J. R. Meteorol. Soc., 134, 1951–1970.doi: 10.1002/qj.339.

Barbosa, P., J. San-Miguel-Ayanz, A. Camia, M. Gimeno, G. Liberta, and G. Schmuck, 2004: Assessment of fire damages in the EU Mediterranean Countries during the 2003 Forest Fire Campaign. Official Publication of the European Commission, S.P.I.04.64, Joint Research Center, Ispra, 2004.

Barré, J., D. Edwards, H. Worden, A. Da Silva, and W. Lahoz, 2015: On the feasibility of monitoring air quality in the lower troposphere from a constellation of northern hemisphere geostationary satellites (Part 1). Atmos. Env, 113, 63-77, doi: 10.1016/j.atmosenv.2015.04.069.

Bencherif, H., L. El Amraoui, N. Semane, S. Massart, D.C. Vidyaranya, A. Hauchecorne, and V.-H. Peuch, 2007: Examination of the 2002 major warming in the southern hemisphere using ground-based and Odin/SMR assimilated data: stratospheric ozone distributions and tropic/mid-latitude exchange. Can. J. Phys., 85, 1287–1300.

Bousserez, N., J.L. Attié, V.-H. Peuch, M. Michou, G. Pfister, D. Edwards, L. Emmons, C. Mari, B. Barret, S.R. Arnold, A. Heckel, A. Richter, H. Schlager, A. Lewis, M. Avery, G. Sachse, E.V. Browell, and J.W. Hair, 2007: Evaluation of the MOCAGE chemistry transport model during the ICARTT/ITOP experiment, J. Geophys. Res., 112, D10S42, doi: 10.1029/2006JD007595.

Buchwitz, M., R. de Beek, S. Noël, J.P. Burrows, H. Bovensmann, O. Schneising, I. Khlystova, M. Bruns, H

785 Bremer, P. Bergamaschi, S. Körner and M. Heimann Atmospheric carbon gases retrieved from
786 SCIAMACHY by WFM-DOAS: version 0.5 CO and CH4 and impact of calibration improvements on
787 CO2 retrieval Atmospheric Chemistry and Physics 6, 2727–2751, 2006
788 Chai, T., and R.R. Draxler, 2014: Root mean square error (RMSE) or mean absolute error (MAE)?
789 Arguments against avoiding RMSE in the literature. Geosci. Model Dev., 7, 1247-1250.
790 Claeyman, M., J.-L. Attié, V.-H. Peuch, L. El Amraoui, W.A. Lahoz, B. Josse, M. Joly, J. Barré, P. Ricaud, S.
791 Massart, A. Piacentini, T. Von Clarmann, M. Höpfner, J. Orphal, J.-M. Flaud and D.P. Edwards, 2011: A
792 thermal infrared instrument onboard a geostationary platform for CO and O_3 measurements in the
793 lowermost troposphere: Observing System Simulation Experiments. Atmos. Meas. Tech., 4, 1637-1661.
794 Courtier, P., C. Freydier, J. Geleyn, F. Rabier, and M. Rochas, 1991: The ARPEGE project at Météo France,
795 in: Atmospheric Models, vol.2, pp. 193–231, Workshop on Numerical Methods, Reading, UK, 1991.
796 Curier, R.L., R. Timmermans, S. Calabretta-Jongen, H. Eskes, A. Segers, D. Swart, and M. Schaap, 2012:
797 Improving ozone forecasts over Europe by synergistic use of the LOTOS-EUROS chemical transport
798 model and in-situ measurements. Atmos. Env., 60, 217-226, doi:10.1016/j.atmosenv.2012.06.017.
799 Cuvelier, C., P. Thunis, R. Vautard, M. Amann, B. Bessagnet M. Bedogni, R. Berkowicz, J. Brandt, F.
800 Brocheton, P. Builtjes, A. Coppalle, B. Denby, G. Douros, A. Graf, O. Hellmuth, C. Honoré, A. Hodzic,
801 J. Jonson, A. Kerschbaumer, F. de Leeuw, E. Minguzzi, N. Moussiopoulos, C. Pertot, G. Pirovano, L.
802 Rouil, M. Schaap, R. Stern, L. Tarrason, E. Vignati, M. Volta, L. White, P. Wind and A. Zuber, 2007:
803 CityDelta: A model intercomparison study to explore the impact of emission reductions in European
804 cities in 2010, Atmos. Env., 41, 189-207, doi: 10.1016/j.atmosenv.2006.07.036.
805 Dufour, A., M. Amodei, G. Ancellet, and V. H. Peuch, 2004: Observed and modeled “chemical weather”
806 during ESCOMPTE. Atmos. Res., 74, 161–189.
807 Edwards, D. P., L. K. Emmons, J. C. Gille, A. Chu, J.-L. Attié, L. Giglio, S. W. Wood, J. Haywood, M. N.
808 Deeter, S. T. Massie, D. C. Ziskin, and J. R. Drummond (2006), Satellite Observed Pollution From
809 Southern Hemisphere Biomass Burning, J. Geophys. Res., 111, D 14312, doi:10.1029/2005JD006655.
810 Edwards, D. P., L. K. Emmons, D. A. Hauglustaine, A. Chu, J. C. Gille, Y. J. Kaufman, G. Pétron, L. N.
811 Yurganov, L. Giglio, M. N. Deeter, V. Yudin, D. C. Ziskin, J. Warner, J.-F. Lamarque, G. L. Francis, S. P.
812 Ho, D. Mao, J. Chan, and J. R. Drummond (2004), Observations of Carbon Monoxide and Aerosol

From the Terra Satellite: Northern Hemisphere Variability, J. Geophys. Res., 109, D24202, doi:10.1029/2004JD0047272004

Edwards, D.P., A.F. Arellano Jr., and M.N. Deeter, 2009: A satellite observation system simulation experiment for carbon monoxide in the lowermost troposphere. J. Geophys. Res., 114, D14304, doi: 10.1029/2008JD011375.

El Amraoui, L., V.-H. Peuch, P. Ricaud, S. Massart, N. Semane, H. Teyssèdre, D. Cariolle, and F. Karcher, 2008a: Ozone loss in the 2002/03 Arctic vortex deduced from the Assimilation of Odin/SMR O_3 and N_2O measurements: N_2O as a dynamical tracer. Q. J. R. Meteorol. Soc., 134, 217–228.

El Amraoui, L., N. Semane, V.-H. Peuch, and M.L. Santee, 2008b: Investigation of dynamical processes in the polar stratospheric vortex during the unusually cold winter 2004/2005. Geophys. Res. Lett., 35, L03803, doi: 10.1029/2007GL031251.

Elbern, H., A. Strunk, and L. Nieradzik, 2010: “Inverse modelling and combined state-source estimation for chemical weather,” in Data Assimilation: Making Sense of Observations, eds W.A. Lahoz, B. Khattatov, and R. Ménard (Berlin: Springer), 491–513.

Emili, E., B. Barret, S. Massart, E. Le Flochmoen, A. Piacentini, L. El Amraoui, O. Pannekoucke, and D. Cariolle, 2014: Combined assimilation of IASI and MLS observations to constrain tropospheric and stratospheric ozone in a global chemical transport model. Atmos. Chem. Phys., 14, 177–198, doi: 0.5194/acp-14-177-2014.

Fitzmaurice, J., and R.L. Bras, 2008: Comparing Reanalyses Using Analysis Increment Statistics. J. Hydrometeor., 9, 1535–1545.

Galli, A., A. Butz, R.A. Scheepmaker, O. Hasekamp, J. Landgraf, P. Tol, D. Wunch, N. M. Deutscher, G.C. Toon, P.O. Wennberg, D.W.T. Griffith, and I. Aben, 2012: CH_4, CO, and H_2O spectroscopy for the Sentinel-5 Precursor mission: an assessment with the Total Carbon Column Observing Network measurements. Atmos. Meas. Tech., 5, 1387-1398.

Gloudemans, A. M. S., Schrijver, H., Hasekamp, O. P., and Aben, I.: Error analysis for CO and CH4 total column retrievals from SCIAMACHY 2.3 μm spectra, Atmos. Chem. Phys., 8, 3999-4017, doi:10.5194/acp-8-3999-2008, 2008.

de Haan, J.F., DISAMAR Algorithms and background, RP-TROPOMI-KNMI-066, KNMI, January 2012.

841 Hass, H., M. van Loon, C. Kessler, R. Stern, J. Matthijsen, F. Sauter, Z. Zlatev, J. Langner, V. Foltescu and
842 M. Schaap, 2003: Aerosol modelling: Results and Intercomparison from European Regional□scale
843 modelling systems, Special Rep. EUROTRAC□2 ISS, Munich, 2003.
844 HTAP, 2007: Hemispheric Transport of Air Pollution 2007, Air Pollution Studies No. 16. UN Publication,
845 ECE/EB.AIR/94, Geneva.
846 Huijnen, V., H.J. Eskes, A. Poupkou, H. Elbern, K.F. Boersma, G. Foret, M. Sofiev, M., et al., 2010:
847 Comparison of OMI NO2 tropospheric columns with an ensemble of global and European regional air
848 quality models. Atmos. Chem. Phys., 10, 3273–3296, doi: 10.5194/acp-10-3273-2010.
849 Jacob, D.J, 2000: Heterogeneous chemistry and tropospheric ozone. Atmos. Env., 34, 2131–2159.
850 Kaiser, J.W., A. Heil, M.O. Andreae, A. Benedetti, N. Chubarova, L. Jones, J.-J. Morcrette, M. Razinger,
851 M.G. Schultz, M. Suttie, and G.R. van der Werf, G. R., 2012: Biomass burning emissions estimated with
852 a global fire assimilation system based on observed fire radiative power. Biogeosciences, 9, 527-554,
853 doi: 10.5194/bg-9-527-2012.
854 Kuenen, J.J.P., A.J.H. Visschedijk, M. Jozwicka, and H.A.C. Denier van der Gon, 2014: TNO-MACC_II
855 emission inventory; a multi-year (2003–2009) consistent high-resolution European emission inventory
856 for air quality modelling. Atmos. Chem. Phys., 14, 10963-10976, doi:10.5194/acp-14-10963-2014,
857 2014.
858 Kujanpää, Jukka, Albert Oude Nijhuis, Henk Eskes, Johan de Haan, Pepijn Veefkind, Johanna Tamminen,
859 Synthetic Observation Product Specification (SOPS), Report of the ESA project "Impact of Spaceborne
860 Observations on Tropospheric Composition Analysis and Forecast" (ISOTROP), 12 August 2015.
861 Lagarde, T., A. Piacentini, and O. Thual, 2001: A new representation of data assimilation methods: the
862 PALM flow charting approach. Q. J. R. Meteorol. Soc., 127, 189–207.
863 Lahoz, W.A., R. Brugge, D.R. Jackson, S. Migliorini, R. Swinbank, D. Lary, et al., 2005: An observing
864 system simulation experiment to evaluate the scientific merit of wind and ozone measurements from the
865 future SWIFT instrument. Q. J. R. Meteorol. Soc., 131, 503–523. doi:10.1256/qj.03.109.
866 Lahoz, W.A., Q. Errera, R. Swinbank, and D. Fonteyn, 2007a: Data assimilation of stratospheric
867 constituents: a review. Atmos. Chem. Phys., 7, 5745–5773, doi: 10.5194/acp-7-5745-2007.
868 Lahoz, W.A., A.J. Geer, S. Bekki, N. Bormann, S. Ceccherini, H. Elbern, Q. Errera, H.J. Eskes, D. Fonteyn,
869 D.R. Jackson, B. Khattatov, M. Marchand, S. Massart, V.-H. Peuch, S. Rharmili, M. Ridolfi, A. Segers,

O. Talagrand, H.E. Thornton, A.F. Vik, and T. von Clarmann, 2007b: The Assimilation of Envisat data (ASSET) project. Atmos. Chem. Phys., 7, 1773–1796.

Lahoz, W.A., V.-H. Peuch, J. Orphal, J.-L. Attié, K. Chance, X. Liu, et al., 2012: Monitoring air quality from space: the case for the geostationary platform. Bull. Am. Meteorol. Soc., 93, 221–233. doi: 10.1175/BAMS-D-11- 00045.1.

Lahoz, W.A., and P. Schneider, 2014: Data assimilation: making sense of earth observation. Front. Environ. Sci., 2, 16. http://dx.doi.org/10.3389/fenvs.2014.00016.

Lee, J.D., A.C. Lewis, P.S. Monks, M. Jacob, J.F. Hamilton, J.R. Hopkins, N.M. Watson, J.E. Saxton, C. Ennis, L.J. Carpenter, N. Carslaw, Z. Fleming, B.J. Bandy, D.E. Oram, S.A. Penkett, J. Slemr, E. Norton, A.R. Rickard, L.K. Whalley, D.E. Heard, W.J. Bloss, T. Gravestock, S.C. Smit, J. Stanton, M.J. Pilling, and M.E. Jenkin, 2006: Ozone photochemistry and elevated isoprene during the UK heatwave of August 2003. Atmos. Env., 40, 7598–7613.

Lefèvre, F., G.P. Brasseur, I. Folkins, A.K. Smith, and P. Simon, 1994: Chemistry of the 1991–1992 stratospheric winter: three dimensional model simulations. J. Geophys. Res., 99, 8183-8195.

Levelt, P., et al., 2009: Observation Techniques and Mission Concepts for Atmospheric Chemistry (CAMELOT), ESA Study, Contract no. 20533/07/NL/HE.

Lord, S.J., E. Kalnay, R. Daley, G.D. Emmitt, and R. Atlas, 1997: “Using OSSEs in the design of the future generation of integrated observing systems, 1st Symposium on Integrated Observing Systems (Long Beach, CA: American Meteorological Society).

Manders, A.M.M., M. Schaap, and R. Hoogerbruggem, 2009: Testing the capability of the chemistry transport model LOTOS-EUROS to forecast PM10 levels in The Netherlands. Atmos. Env., 4050-459 doi:10.1016/j.atmosenv.2009.05.006.

Marécal, V., V.-H. Peuch, C. Andersson, S. Andersson, J. Arteta, M. Beekmann, A. Benedictow, R. Bergström, B. Bessagnet, A. Cansado, F. Chéroux, A. Colette, A. Coman, R.L. Curier, H.A.C. Denier van der Gon, A. Drouin, H. Elbern, E. Emili, R.J. Engelen, H.J. Eskes, G. Foret, E. Friese, M. Gauss, C. Giannaros, J. Guth, M. Joly, E. Jaumouillé, B. Josse, N. Kadygrov, J.W. Kaiser, K. Krajsek, J. Kuenen, U. Kumar, N. Liora, E. Lopez, L. Malherbe, I. Martinez, D. Melas, F. Meleux, L. Menut, P. Moinat, T. Morales, J. Parmentier, A. Piacentini, M. Plu, A. Poupkou, S. Queguiner, L. Robertson, L. Rouïl, M. Schaap, A. Segers, M. Sofiev, M. Thomas, R. Timmermans, Á. Valdebenito, P. van Velthoven, R. van

899 Versendaal, J. Vira, and A. Ung, 2015: A regional air quality forecasting system over Europe: the
900 MACC-II daily ensemble production, Geosci. Model Dev., 8, 2777-2813, doi:10.5194/gmd-8-2777-
901 2015
902 Massart, S., C. Clerbaux, D. Cariolle, A. Piacentini, S. Turquety, and J. Hadji- Lazaro, 2009: First steps
903 towards the assimilation of IASI ozone data into the MOCAGE-PALM system. Atmos. Chem. Phys., 9,
904 5073–5091.doi: 10.5194/acp- 9-5073-2009.
905 Masutani, M., T.W. Schlatter, R. M. Errico, A. Stoffelen, E. Andersson, W. Lahoz, J.S. Woollen, G.D.
906 Emmitt, L.-P. Riishøjgaard, and S. J. Lord, 2010a: Observing system simulation experiments. Data
907 Assimilation: Making Sense of Observations, W. A. Lahoz, B. Khattatov and R. Ménard, Eds., Springer,
908 647-679.
909 Masutani, M., J.S. Woollen, S.J. Lord, G.D. Emmitt, T.J. Kleespies, S.A. Wood, S. Greco, H. Sun, J. Terry, V.
910 Kapoor, R. Treadon, and K.A. Campana, 2010b: Observing system simulation experiments at the
911 National Centers for Environmental Prediction. J. Geophys. Res., 115, doi: 10.1029/2009JD012528.
912 Nitta, T., 1975: Some analyses of observing systems simulation experiments in relation to First GARP
913 Global Experiment, in GARP Working Group on Numerical Experimentation, Report No. 10,US GARP
914 Plan (Washington, DC), 1–35.
915 Ordoñez, C., N. Elguindi, O. Stein, V. Huijnen, J. Flemming, A. Inness, H. Flentje, E. Katragkou, P. Moinat,
916 V.-H. Peuch, A. Segers, V. Thouret, G. Athier, M. van Weele, C. S. Zerefos, J.-P. Cammas, and M.G.
917 Schultz, 2010: Global model simulations of air pollution during the 2003 European heat wave. Atmos.
918 Chem. Phys., 10, 789-815.
919 Peuch, V.-H., M. Amodei, T. Barthet, M.L. Cathala, M. Michou, and P. Simon, 1999: MOCAGE, MOdéle de
920 Chimie Atmosphérique à Grande Echelle, in: Proceedings of Météo France: Workshop on atmospheric
921 modelling, pp. 33–36, Toulouse, France, 1999.
922 Rodgers, C. D., Inverse methods for atmospheric sounding: Theory and Practice, Series on Atmospheric,
923 Oceanic and Planetary Physics–Vol. 2., Singapore, World Scientific, 2000.
924 Schaap, M., R.M.A. Timmermans, M. Roemer, G.A.C. Boersen, P.J.H. Builtjes, F.J. Sauter, G.J.M. Velders,
925 and J.P. Beck, 2008: The Lotos-Euros model: Description, validation and latest developments.
926 International Journal of Environment and Pollution, 32, 270–290.

927 Semane, N., V.-H. Peuch, L. El Amraoui, H. Bencherif, S. Massart, D. Cariolle, J.-L. Attié, and R. Abida,
928 2007: An observed and analysed stratospheric ozone intrusion over the high Canadian Arctic UTLS
929 region during the summer of 2003, Q. J. R. Meteorol. Soc., 133, 171–178, doi: 10.1002/qj.141.
930 Solberg, S., Ø Hov, A. Søvde, I.S.A. Isaksen, P. Coddeville, H. De Backer, C. Forster, Y. Orsolini, and K.
931 Uhse, 2008: European surface ozone in the extreme summer 2003, J. Geophys. Res., 113, D07307, doi:
932 10.1029/2007JD009098.
933 Stockwell, W.R., F. Kirhcner, M. Kuhn, and S. Seefeld, 1997: A new mechanism for regional atmospheric
934 chemistry modeling. J. Geophys. Res., 102, 25847-25879, doi: 10.1029/97JD00849.
935 Stoffelen, A., G.J. Marseille, F. Bouttier, D. Vasiljevic, S. DeHaan, and C. Cardinali, 2006: ADM-Aeolus
936 Doppler wind lidar observing system simulation experiment. Q. J. R. Meteorol. Soc., 619, 1927–1948.
937 doi:10.1256/qj.05.83.
938 Stern, R., P. Builtjes, M. Schaap, R. Timmermans, R. Vautard, A. Hodzic, M. Memmesheimer, H. Feldmann,
939 E. Renner, R. Wolke, and A. Kerschbaumer, 2008: A model inter-comparison study focussing on
940 episodes with elevated PM10 concentrations. Atmos. Env., 42, 4567-4588. http://dx.doi.org/
941 10.1016/j.atmosenv.2008.01.068.
942 Streets D. G., 2013: Emissions estimation from satellite retrievals: A review of current capability
943 Atmospheric Environment, 77 1011-1042
944 Tan, D.G.H., E. Andersson, M. Fisher, and L. Isaksen, 2007: Observing system impact assessment using a
945 data assimilation ensemble technique: application to the ADM-Aeolus wind profiling mission. Q. J. R.
946 Meteorol. Soc., 133, 381–390. doi: 10.1002/qj.43.
947 Tangborn, A., I. Štajner, M. Buchwitz, I. Khlystova, S. Pawson, R. Hudman, et al., 2009: Assimilation of
948 SCIAMACHY total column CO observations: global and regional analysis of data impact. J. Geophys.
949 Res., 114. doi: 10.1029/2008JD010781.
950 Teyssèdre, H., M. Michou, H.L. Clark, B. Josse, F. Karcher, D. Olivié, V.-H. Peuch, D. Saint-Martin, D.
951 Cariolle,, J.-L. Attié, P. Nédélec, P. Ricaud, V. Thouret, A.R.J. van der A,, A. Volz-Thomas, and F.
952 Chéroux, F., 2007: A new tropospheric and stratospheric Chemistry and Transport Model MOCAGE-
953 Climat for multi-year studies: evaluation of the present-day climatology and sensitivity to surface
954 processes. Atmos. Chem. Phys., 7, 5815–5860, http://www.atmos-chem-phys.net/7/5815/2007/.

955 Timmermans, R.M.A., M. Schaap, H. Elbern, R. Siddans, S. Tjemkes, R. Vautard, et al., 2009a: An
956 Observing System Simulation Experiment (OSSE) for Aerosol Optical Depth from Satellites. J. Atmos.
957 Ocean Tech., 26, 2673–2682. doi: 10.1175/2009JTECHA1263.1.
958 Timmermans, R.M.A., AJ. Segers, P.J.H. Builtjes, R. Vautard, R. Siddans, H. Elbern, et al., 2009b: The
959 added value of a proposed satellite imager for ground level particulate matter analyses and forecasts.
960 IEEE J. Sel. Top. Appl. 2, 271–283. doi:10.1109/JSTARS.2009.2034613.
961 Timmermans, R., W.A. Lahoz, J.-L. Attié, V.-H. Peuch, L. Curier, D. Edwards, H. Eskes, and P. Builtjes,
962 2015: Observing System Simulation Experiments for Air Quality. Atmos. Env., 115, 199-213,
963 doi:10.1016/j.atmosenv.2015.05.032.
964 Tressol, M., C. Ordoñez, R. Zbinden, J. Brioude, V. Thouret, C. Mari, P. Nedélec, J.-P. Cammas, H. Smit, H.-
965 W. Patz, and A. Volz-Thomas, 2008: Air pollution during the 2003 European heat wave as seen by
966 MOZAIC airliners. Atmos. Chem. Phys., 8, 2133-2150.
967 Vautard, R., C. Honoré, M. Beekmann, and L. Rouïl, 2005: Simulation of ozone during the August 2003 heat
968 wave and emission control scenarios. Atmos. Env., 39, 2957–2967.
969 van Loon, M., R. Vautard, M. Schaap, R. Bergstrom, B. Bessagnet, J. Brandt, P.J.H. Builtjes, J.H.
970 Christensen, C. Cuvelier, A. Graff, J.E. Jonson, M. Krol, J. Langner, P. Roberts, L. Rouïl, R. Stern, L.
971 Tarrason, P. Thunis, E. Vignati, and L. White, 2007: Evaluation of long□term ozone simulations from
972 seven regional air quality models and their ensemble, Atmos. Env., 41, 2083□2097. doi:
973 10.1016/j.atmosenv.2006.10.073.
974 Veefkind, J.P., I. Aben, K. McMullan, H. Förster, J. de Vries, G. Otter, J. Claas, H.J. Eskes, J.F. de Haan, Q.
975 Kleipool, M. van Weele, O. Hasekamp, R. Hoogeveen, J. Landgraf, R. Snel, P. Tol, P. Ingmann, R.
976 Voors, B. Kruizinga, R. Vink, H. Visser, and P.F. Levelt, 2012: TROPOMI on the ESA Sentinel-5
977 Precursor: A GMES mission for global observations of the atmospheric composition for climate, air
978 quality and ozone layer applications. Remote Sens. Env., 120, 70-83.
979 Weaver, A., and P. Courtier, 2001: Correlation modelling on the sphere using a generalized diffusion
980 equation. Q. J. R. Meteorol. Soc., 127, 1815–1846.
981 Willmott, C., and K. Matsuura, 2005: Advantages of the Mean Absolute Error (MAE) over the Root Mean
982 Square Error (RMSE) in assessing average model performance. Clim. Res., 30, 79-82.

983 Willmott, C., K. Matsuura, and S.M. Robeson, 2009: Ambiguities inherent in sums-of-squares-based error
984 statistics. Atmos. Env., 43, 749-752.

985 Worden, H. M., M. N. Deeter, Christian Frankenberg, Maya George, Florian Nichitiu, John Worden,
986 Ilse Aben et al. "Decadal record of satellite carbon monoxide observations." Atmospheric Chemistry
987 and Physics 13, no. 2 (2013): 837-850.

988 Yumimoto, K., 2013: Impacts of geostationary satellite measurements on CO forecasting: an observing
989 system simulation experiment with GEOS- Chem/LETKF data assimilation system. Atmos. Env., 74,
990 123–133. doi: 10.1016/j.atmosenv.2013.03.032.

991 Zoogman, P., D.J. Jacob, K. Chance, L. Zhang, P. Le Sager, A.M. Fiore, A. Eldering, X. Liu, V. Natraj, and
992 S.S. Kulawik, 2011. Ozone air quality measurement requirements for a geostationary satellite mission.
993 Atmos. Env., 45, 7143-7150.

994 Zoogman, P., D.J. Jacob, K. Chance, X. Liu, M. Lin, A.M. Fiore, and K. Travis, 2014a. Monitoring high-
995 ozone events in the US Intermountain West using TEMPO geostationary satellite observations. Atmos.
996 Chem. Phys., 14, 6261-6271. http://dx.doi.org/10.5194/acp-14-6261-2014.

997 Zoogman, P., D.J. Jacob, K. Chance, H.M. Worden, D.P. Edwards, and L. Zhang, 2014b: Improved
998 monitoring of surface ozone by joint assimilation of geostationary satellite observations of ozone and
999 CO. Atmos. Env., 84, 254-261. http://dx.doi.org/10.1016/j.atmosenv.2013.11.048.

1000
1001
1002
1003
1004
1005
1006
1007

Atmos. Chem. Phys. Discuss., doi:10.5194/acp-2015-924, 2016
Manuscript under review for journal Atmos. Chem. Phys.
Published: 1 February 2016

1008 # Tables

1009

1010 **Table 1:** Spectral and radiometric settings for DISAMAR, and the look-up table nodes.

Spectral and radiometric settings	
Spectral range [nm]	2330-2345
Spectral resolution (FWHM) [nm]	0.25
Spectral sampling [nm]	0.1
SNR Earth radiance	120
SNR Solar irradiance	5000
Additional calibration error (%)	1.0, correlation length 100 nm
Node points	
cos(SZA)	0.1 - 1.0, step 0.1
cos(VZA)	0.3 - 1.0, step 0.1
Relative azimuth [degree]	0.0, 180.0
Cloud/surface pressure	1100 - 200, step -100
Cloud/surface albedo	0.0, 0.005, 0.01, 0.02, 0.04, 0.06, 0.1, 0.2, 0.3, 0.4, 0.8, 0.9
Pressure layers	1100, 1000, 900, 800, 700, 600, 500, 400, 300, 200, 137.50, 68.75, 34.38, 17.19, 8.59, 4.30, 2.15, 1.07, 0.54, 0.27, 0.13, 0.07

1011

1012

1013

1014

Atmos. Chem. Phys. Discuss., doi:10.5194/acp-2015-924, 2016
Manuscript under review for journal Atmos. Chem. Phys.
Published: 1 February 2016

Atmospheric Chemistry and Physics Discussions

1015

1016 **Table 2**: Description of the configuration used in the assimilation system

	Description
Assimilation	3D-var, 1 hour window
Background standard deviation	in % of the background field (vertically variable)
Background correlation zonal Length scale (L_x)	constant 35 km
Background correlation meridional length scale (L_y)	constant 35 km
Background correlation vertical length scale (L_z)	one vertical model layer
S-5P total column CO observation errors	from retrieval product and weighting to account for the total column

1017

1018

1019

1020

1021

1022

1023

1024

1025

1026

1027

1028

Atmos. Chem. Phys. Discuss., doi:10.5194/acp-2015-924, 2016
Manuscript under review for journal Atmos. Chem. Phys.
Published: 1 February 2016

Atmospheric Chemistry and Physics Discussions

Figures

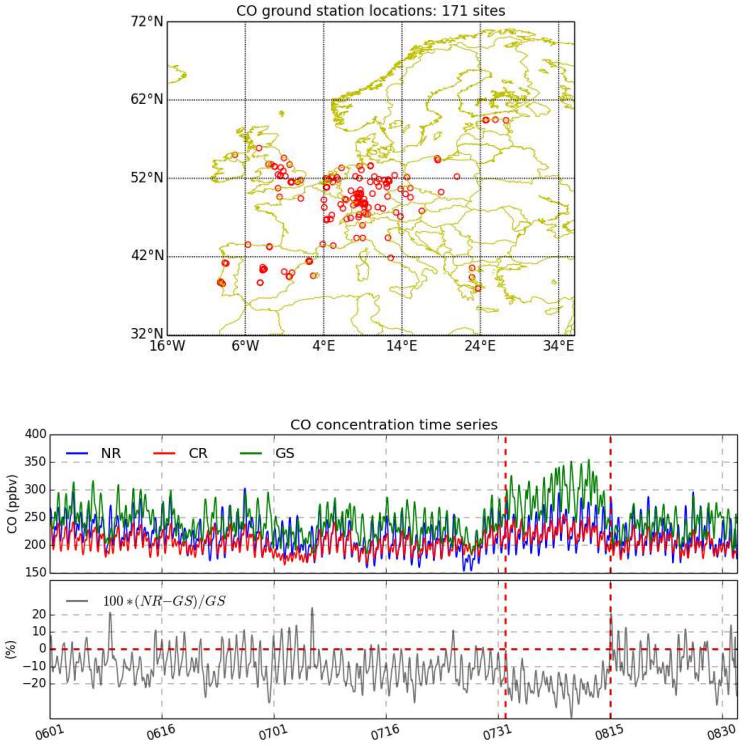

Figure 1: Top panel: location of selected ground-based stations for CO measurements taken from the Airbase database during northern summer 2003 (1 June – 31 August). There are 171 sites with locations shown by circles. The labels show longitude, degrees (x-axis) by latitude, degrees (y-axis). Middle panel: simulated and measured time-series of CO concentrations in surface air from nature run (blue line), the control run (red line) and from the selected 171 Airbase sites (green line). We form the CO time-series for the ground-based stations by averaging the hourly data representative of the 171 sites. The labels show time in MMDD format (x-axis) by CO concentration, parts per billion by volume, ppbv (y-axis). Bottom panel: The gray curve shows the relative error of the nature run with respect to the observations, defined as NR value minus ground station value divided by the ground station value and multiplied by 100. The labels show time in MMDD format (x-axis) by relative error, percent (y-axis). The vertical red dashed lines in the middle and bottom panels delineate the 2003 European heat wave period (31 July – 15 August).

Atmos. Chem. Phys. Discuss., doi:10.5194/acp-2015-924, 2016
Manuscript under review for journal Atmos. Chem. Phys.
Published: 1 February 2016

Atmospheric Chemistry and Physics Discussions

1056

1057

1058

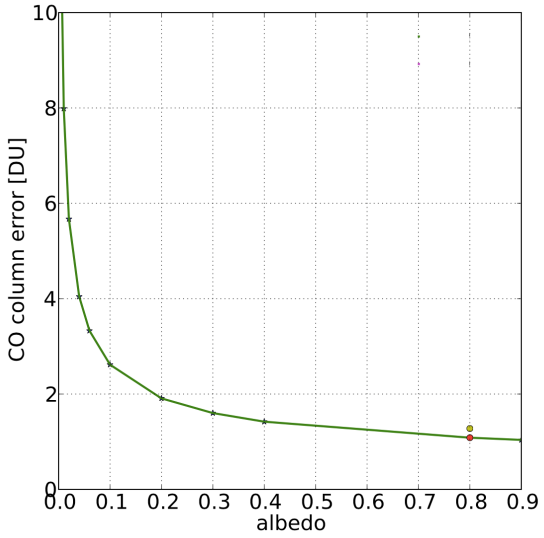

Figure 2: Dependence of the CO column uncertainty on the surface albedo. Simulation settings are: solar zenith angle 53 degrees, viewing zenith angle 26 degrees, relative azimuth angle 0 degree, cloud/surface pressure 1100 hPa.

1059

1060

1061

1062

1063

1064

1065

1066

Atmos. Chem. Phys. Discuss., doi:10.5194/acp-2015-924, 2016
Manuscript under review for journal Atmos. Chem. Phys.
Published: 1 February 2016

1067

1068

1069

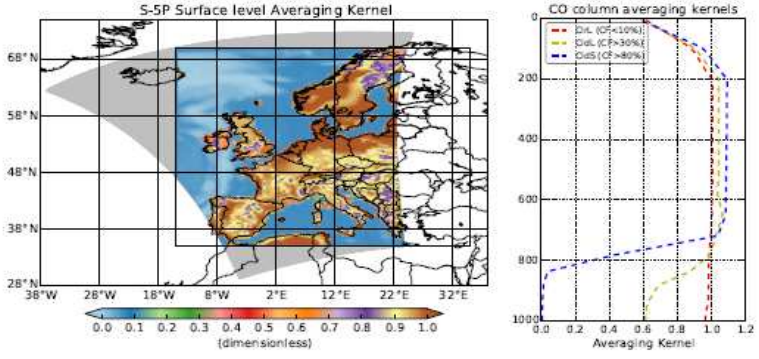

1077

1078 **Figure 3:** Left panel: S-5P CO averaging kernel values at the surface. Labels are longitude, degrees (x-axis)
1079 by latitude, degrees (y-axis). Right panel: Averaging kernels for land pixels with cloud fraction less than 10%
1080 (dashed red lines); for land pixels with cloud fraction greater than 30% (dashed yellow lines); and for sea
1081 pixels with cloud fraction greater than 80% (dashed blue lines). The averaging kernels are for an average of
1082 the data shown on the swath for 1 June 2003 at 12:34 UTC. Labels are averaging kernel, normalized (x-axis)
1083 by pressure level, hPa (y-axis).

1084

1085

1086

1087

1088

1089

1090

1091

1092

1093

1094

Atmos. Chem. Phys. Discuss., doi:10.5194/acp-2015-924, 2016
Manuscript under review for journal Atmos. Chem. Phys.
Published: 1 February 2016

Atmospheric Chemistry and Physics Discussions

1095

1096

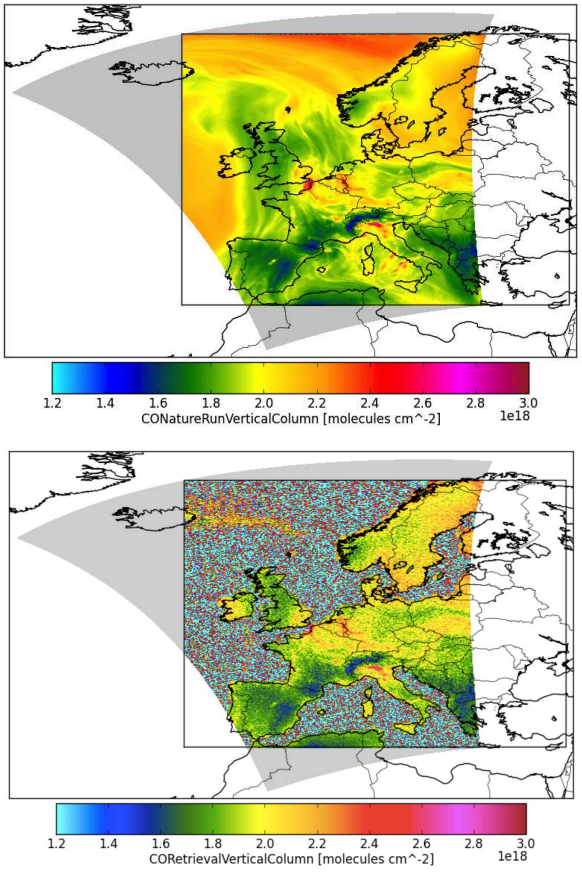

Figure 4: Top: Nature run collocated to the synthetic S-5P observations for the 12:34 orbit on 1 June 2003. Bottom: corresponding synthetic observations.

1097

1098

1099

1100

1101

1102

1103

Atmos. Chem. Phys. Discuss., doi:10.5194/acp-2015-924, 2016
Manuscript under review for journal Atmos. Chem. Phys.
Published: 1 February 2016

Atmospheric Chemistry and Physics Discussions

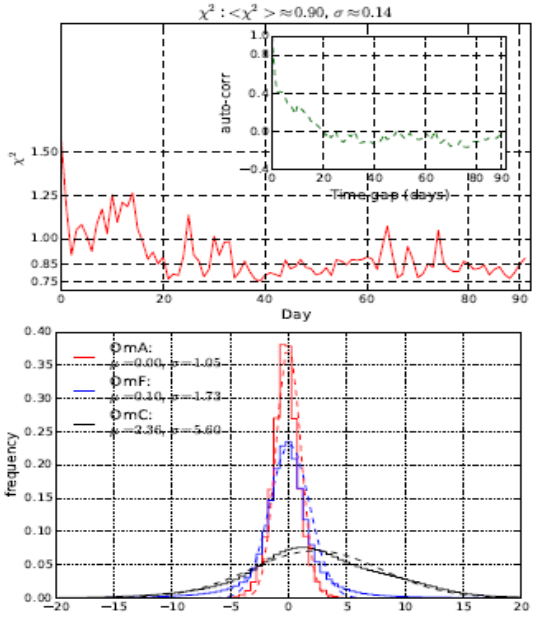

Figure 5: Self-consistency tests. Top panel: time-series (red line) of χ^2 for OmF and its associated auto-correlation signal (green line). For the χ^2 diagnostic we normalize the OmF differences by the background error. The labels show time, days (x-axis) and χ^2 value (y-axis) for the χ^2 plot, and time gap, days (x-axis) and auto-correlation (y-axis) for the auto-correlation plot. Bottom panel: histograms of Observations minus Analysis (OmA -red solid line), Observations minus Forecast (OmF -blue solid line), and Observations minus Control run (OmC -black solid line). We normalize these differences by the observation error. The dashed lines correspond to the Gaussian fits of the different histograms. The labels show the OmA, OmF or OmC differences (x-axis) and the frequency of occurrence of the differences (y-axis). We calculate the diagnostics OmA, OmF, and OmC over the period of 1 June – 31 August 2003.

Atmos. Chem. Phys. Discuss., doi:10.5194/acp-2015-924, 2016
Manuscript under review for journal Atmos. Chem. Phys.
Published: 1 February 2016

Atmospheric Chemistry and Physics Discussions

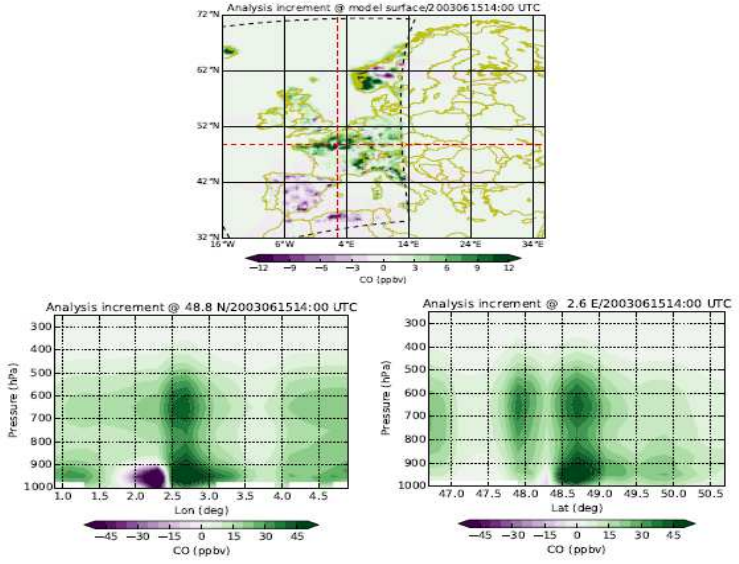

Figure 6: S-5P CO analysis increments, units of ppbv, at 14:00 UTC on 15 June 2003: Top panel: geographical distribution at the model surface. Red dashed lines show zonal and meridional vertical slices at 48°8 N, and 2°6 E, respectively. The black dashed line shows the S-5P cross-track at 13:12 UTC, clipped to fit the OSSE simulation domain. Note that we measure the S-5P CO observations at 13:12 UTC. The labels show longitude, degrees (x-axis) and latitude, degrees (y-axis). Left and right bottom panels show, respectively, the longitude-height and latitude-height cross-sections at a location near Paris. The labels for the bottom panels show longitude, degrees (x-axis, left panel), latitude, degrees (x-axis, right panel), and pressure, hPa (y-axis, both panels). Green/purple colours indicate positive/negative values in the increment fields.

Atmos. Chem. Phys. Discuss., doi:10.5194/acp-2015-924, 2016
Manuscript under review for journal Atmos. Chem. Phys.
Published: 1 February 2016

Atmospheric Chemistry and Physics Discussions

1158

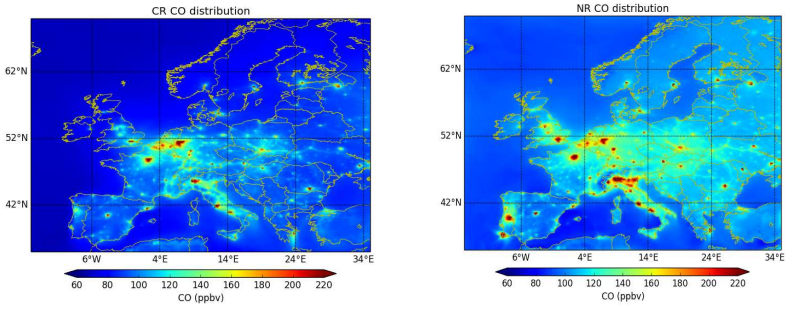

1159

1160 **Figure 7:** Distribution of CO surface concentrations, units ppbv, averaged for the period 1 June – 31 August
1161 2003. Top left panel: the control run (CR) from MOCAGE; right top panel: the nature run (NR) from
1162 LOTOS-EUROS; bottom panel: the assimilation run (AR) from MOCAGE obtained after assimilating the S-
1163 5P CO total column simulated data sampled from the NR. In all panels, the labels show longitude, degrees
1164 (x-axis) and latitude, degrees (y-axis). Red/blue colours indicate relatively high/low values of the CO surface
1165 concentrations.

1166

1167

1168

1169

1170

1171

1172

1173

1174

Atmos. Chem. Phys. Discuss., doi:10.5194/acp-2015-924, 2016
Manuscript under review for journal Atmos. Chem. Phys.
Published: 1 February 2016

Atmospheric Chemistry and Physics Discussions

1175

1176

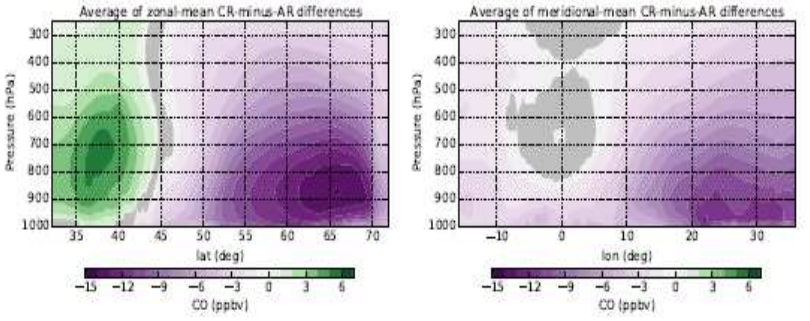

1183

1184 **Figure 8:** Zonal (left panel) and meridional (right panel) slices of the difference between the CR and AR CO
1185 fields, units of ppbv, averaged over the summer period (1 June – 31 August 2003). The areas highlighted in
1186 grey colour indicate where the AR is not significantly different to the CR at the 99% confidence level. The
1187 labels in the left panel are latitude, degrees (x-axis) and pressure, hPa (y-axis). The labels in the right panel
1188 are longitude, degrees (x-axis) and pressure, hPa (y-axis). Green/purple colours indicate positive/negative
1189 values in the difference fields.

1190

1191

1192

1193

1194

1195

1196

1197

1198

1199

1200

1201

1202

Atmos. Chem. Phys. Discuss., doi:10.5194/acp-2015-924, 2016
Manuscript under review for journal Atmos. Chem. Phys.
Published: 1 February 2016

Atmospheric Chemistry and Physics Discussions

1203

1204

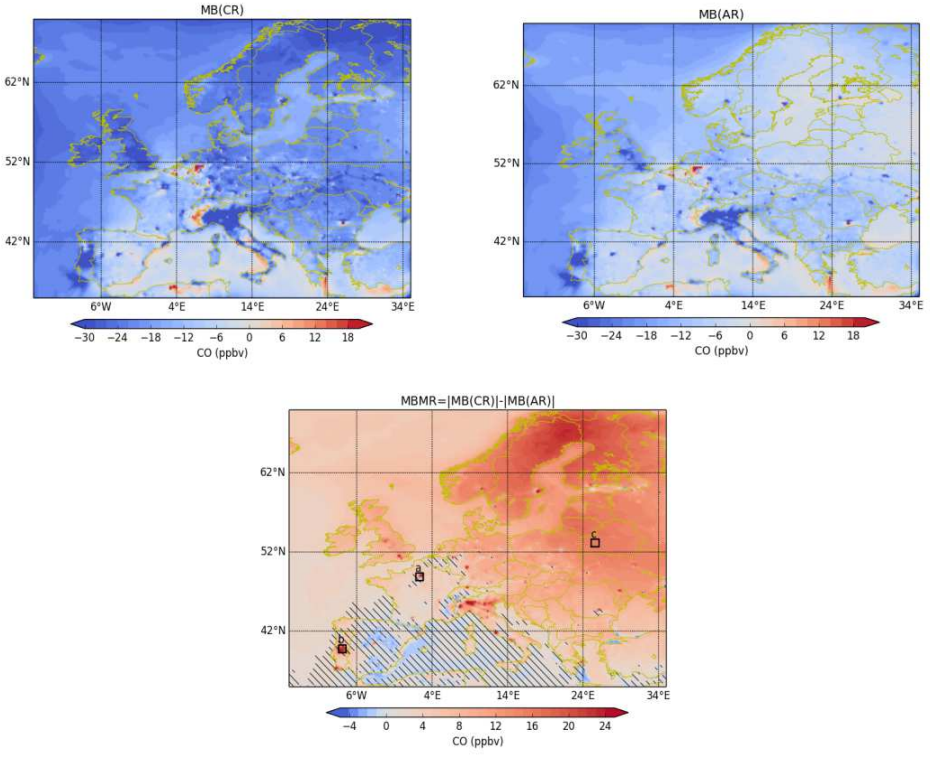

1205

1206 **Figure 9:** Mean bias reduction at the surface for CO, units of ppbv: Left top panel shows the CR mean bias
1207 with respect to the NR (CR-NR). Right top panel shows the AR mean bias with respect to the NR (AR-NR).
1208 Bottom panel shows the mean bias magnitude reduction (absolute value of the mean bias for CR minus the
1209 absolute value of the mean bias for AR). We average the data over northern summer 2003 (1 June – 31
1210 August). The labels show longitude, degrees (x-axis) and latitude, degrees (y-axis). The hatched area in the
1211 bottom panel shows where the mean bias plotted in this panel (MBMR) is not statistically significant at the
1212 99% confidence level. The three squares in the bottom panel represent locations for the three time-series
1213 shown in Fig. 12. Red/blue colours indicate positive/negative values in the MB/MBMR.

1214

1215

1216

1217

Atmos. Chem. Phys. Discuss., doi:10.5194/acp-2015-924, 2016
Manuscript under review for journal Atmos. Chem. Phys.
Published: 1 February 2016

Atmospheric Chemistry and Physics Discussions

1218

1219

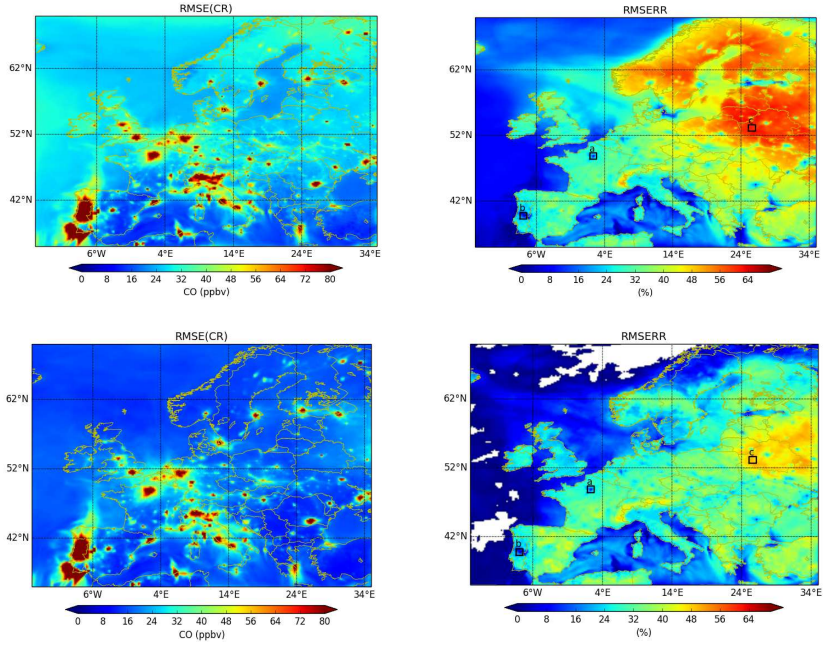

1220

1221

1222 **Figure 10:** Top: Root Mean Square Error (RMSE), units of ppbv, between CR and NR (left panel), and its
1223 corresponding reduction rate RMSERR, in % (right panel) keeping the systematic error. Bottom: Same as top
1224 panel but calculating the RMSE after removing the systematic error. The labels on each panel are longitude,
1225 degrees (x-axis) and latitude, degrees (y-axis). The three squares in the two right panels represent locations
1226 for the three time-series shown in Fig. 12. Red/blue colours indicate relatively high/low values in the
1227 RMSE/RMSERR.

1228

1229

1230

1231

1232

1233

1234

1235

Atmos. Chem. Phys. Discuss., doi:10.5194/acp-2015-924, 2016
Manuscript under review for journal Atmos. Chem. Phys.
Published: 1 February 2016

Atmospheric Chemistry and Physics Discussions

1236

1237

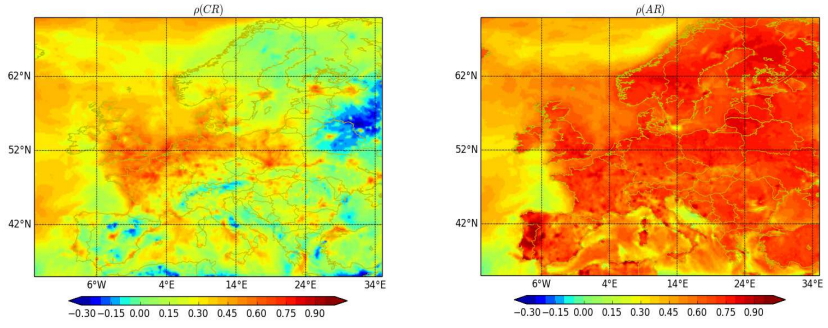

1238

1239 **Figure 11:** Correlation coefficient between the CR and the NR (left panel) and the AR and the NR (right
1240 panel) at the surface and for the northern summer period (1 June – 31 August). The labels are longitude,
1241 degrees (x-axis) and latitude, degrees (y-axis). Red/blue colours indicate positive/negative values of the
1242 correlation coefficient.

1243

1244

1245

1246

1247

1248

1249

1250

1251

1252

1253

1254

1255

1256

1257

Atmos. Chem. Phys. Discuss., doi:10.5194/acp-2015-924, 2016
Manuscript under review for journal Atmos. Chem. Phys.
Published: 1 February 2016

Atmospheric Chemistry and Physics Discussions

1258

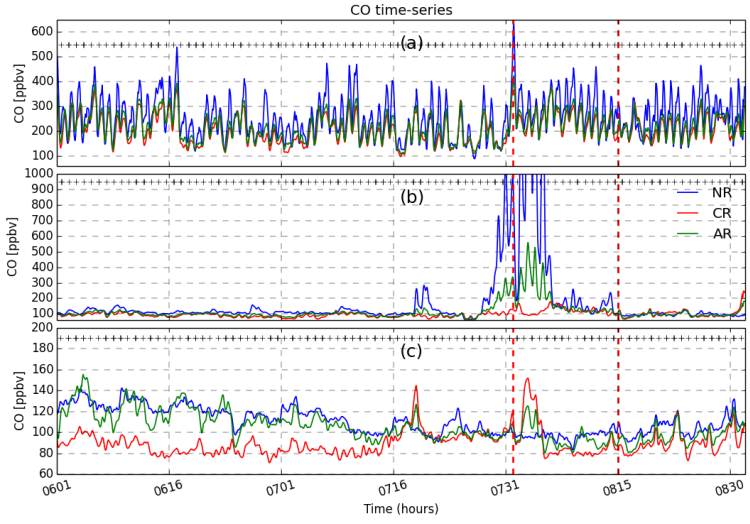

1259

1260 **Figure 12:** Time-series for CO surface concentrations (1 June – 31 August) from NR (blue colour), CR (red
1261 colour) and AR (green colour) over three different locations represented by squares in Figs. 9 and 10. Top
1262 panel: area near Paris; middle panel: area over Portugal, where forest fires occurred; bottom panel: Eastern
1263 part of the study domain. The labels in the three panels are time, in format MMDD (x-axis) and CO
1264 concentration, ppbv (y-axis). The plus symbols at the top of each panel indicate availability of observations
1265 from the S-5P platform.

1266

1267

1268

1269

1270

1271

1272

1273

1274

1275

Atmos. Chem. Phys. Discuss., doi:10.5194/acp-2015-924, 2016
Manuscript under review for journal Atmos. Chem. Phys.
Published: 1 February 2016

1276

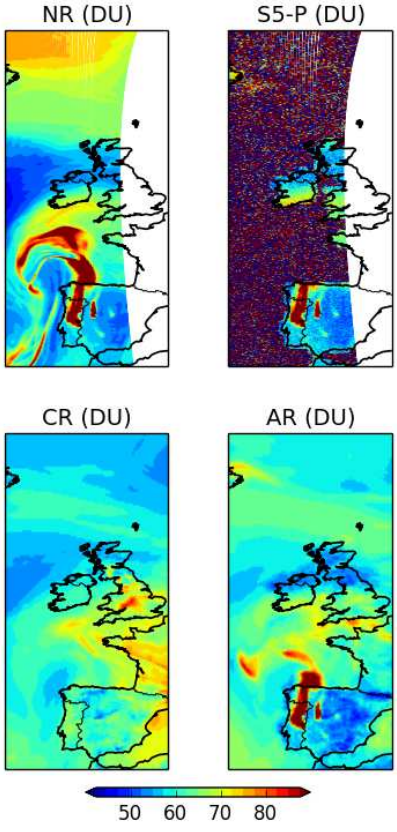

1277

1278 **Figure 13:** CO total column at 14:15 UTC on 4 August 2003, Dobson units, DU. Top left panel: NR; top
1279 right panel: simulated S-5P observations; bottom left panel: CR; bottom right panel: AR. Red/blue colours
1280 indicate relatively high/low values of the CO total column.

1281

1282

1283

1284

1285

1286

1287

1288

Atmos. Chem. Phys. Discuss., doi:10.5194/acp-2015-924, 2016
Manuscript under review for journal Atmos. Chem. Phys.
Published: 1 February 2016

Atmospheric Chemistry and Physics Discussions

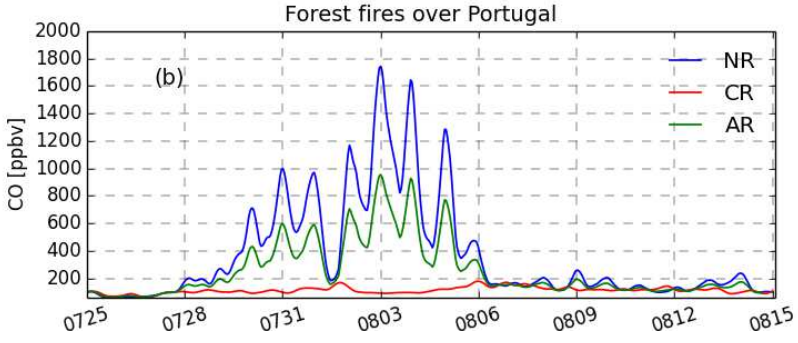

Figure 14: Time-series for CO surface concentrations for the period covering the Portugal forest fires (25 July – 15 August) from NR (blue colour), CR (red colour) and AR (green colour) over the location associated with the middle panel of Fig.12. These data concern the second OSSE we perform to understand the behaviour of the original OSSE over the period of the forest fires (see text for more details). The labels are time, in format MMDD (x-axis) and CO concentration, ppbv (y-axis).